

Euclid Quick Data Release (Q1)

LEMON – Lens Modelling with Neural networks. Automated and fast modelling of *Euclid* gravitational lenses with a singular isothermal ellipsoid mass profile

Euclid Collaboration: V. Busillo^{*1,2,3}, C. Tortora¹, R. B. Metcalfe^{4,5}, J. W. Nightingale⁶, M. Meneghetti^{5,7}, F. Gentile^{8,5,9}, R. Gavazzi^{10,11}, F. Zhong¹², R. Li¹³, B. Clément^{14,15}, G. Covone^{2,1,3}, N. R. Napolitano^{16,1,3}, F. Courbin^{17,18}, M. Walmsley^{19,20}, E. Jullo¹⁰, J. Pearson²¹, D. Scott²², A. M. C. Le Brun²³, L. Leuzzi^{4,5}, N. Aghanim²⁴, B. Altieri²⁵, A. Amara²⁶, S. Andreon²⁷, H. Aussel²⁸, C. Baccigalupi^{29,30,31,32}, M. Baldi^{9,5,7}, S. Bardelli⁵, P. Battaglia⁵, A. Biviano^{30,29}, E. Branchini^{33,34,27}, M. Brescia^{2,1}, J. Brinchmann^{35,36}, S. Camera^{37,38,39}, G. Cañas-Herrera^{40,41,42}, V. Capobianco³⁹, C. Carbone⁴³, V. F. Cardone^{44,45}, J. Carretero^{46,47}, S. Casas⁴⁸, M. Castellano⁴⁴, G. Castignani⁵, S. Cavuoti^{1,3}, K. C. Chambers⁴⁹, A. Cimatti⁵⁰, C. Colodro-Conde⁵¹, G. Congedo⁵², C. J. Conselice²⁰, L. Conversi^{53,25}, Y. Copin⁵⁴, H. M. Courtois⁵⁵, M. Cropper⁵⁶, A. Da Silva^{57,58}, H. Degaudenzi⁵⁹, S. de la Torre¹⁰, G. De Lucia³⁰, A. M. Di Giorgio⁶⁰, J. Dinis^{57,58}, H. Dole²⁴, F. Dubath⁵⁹, X. Dupac²⁵, S. Dusini⁶¹, S. Escoffier⁶², M. Farina⁶⁰, R. Farinelli⁵, F. Faustini^{63,44}, S. Ferriol⁵⁴, F. Finelli^{5,64}, S. Fotopoulou⁶⁵, M. Frailis³⁰, E. Franceschi⁵, S. Galeotta³⁰, K. George⁶⁶, W. Gillard⁶², B. Gillis⁵², C. Giocoli^{5,7}, J. Gracia-Carpio⁶⁷, B. R. Granett²⁷, A. Grazian⁶⁸, F. Grupp^{67,66}, S. V. H. Haugan⁶⁹, W. Holmes⁷⁰, I. Hook⁷¹, F. Hormuth⁷², A. Hornstrup^{73,74}, P. Hudelot¹¹, K. Jahnke⁷⁵, M. Jhabvala⁷⁶, B. Joachimi⁷⁷, E. Keihänen⁷⁸, S. Kermiche⁶², A. Kiessling⁷⁰, B. Kubik⁵⁴, M. Kümmel⁶⁶, M. Kunz⁷⁹, H. Kurki-Suonio^{80,81}, Q. Le Boulc’h⁸², S. Ligi³⁹, P. B. Lilje⁶⁹, V. Lindholm^{80,81}, I. Lloro⁸³, G. Mainetti⁸², D. Maino^{84,43,85}, E. Maiorano⁵, O. Mansutti³⁰, O. Marggraf⁸⁶, K. Markovic⁷⁰, M. Martinelli^{44,45}, N. Martinet¹⁰, F. Marulli^{4,5,7}, R. Massey⁸⁷, S. Maurogordato⁸⁸, E. Medinaceli⁵, S. Mei^{89,90}, Y. Mellier^{91,11}, E. Merlin⁴⁴, G. Meylan¹⁴, A. Mora⁹², M. Moresco^{4,5}, L. Moscardini^{4,5,7}, R. Nakajima⁸⁶, C. Neissner^{93,47}, S.-M. Niemi⁴⁰, C. Padilla⁹³, S. Paltani⁵⁹, F. Pasian³⁰, K. Pedersen⁹⁴, V. Pettorino⁴⁰, S. Pires²⁸, G. Polenta⁶³, M. Poncet⁹⁵, L. A. Popa⁹⁶, L. Pozzetti⁵, F. Raison⁶⁷, R. Rebolo^{51,97,98}, A. Renzi^{99,61}, J. Rhodes⁷⁰, G. Riccio¹, E. Romelli³⁰, M. Roncarelli⁵, R. Saglia^{66,67}, Z. Saki^{100,101,102}, A. G. Sánchez⁶⁷, D. Sapone¹⁰³, B. Sartoris^{66,30}, J. A. Schewtschenko⁵², M. Schirmer⁷⁵, P. Schneider⁸⁶, T. Schrabback¹⁰⁴, A. Secroun⁶², E. Sefusatti^{30,29,31}, G. Seidel⁷⁵, M. Seiffert⁷⁰, S. Serrano^{105,106,107}, P. Simon⁸⁶, C. Sirignano^{99,61}, G. Sirri⁷, G. Smadja⁵⁴, L. Stanco⁶¹, J. Steinwagner⁶⁷, P. Tallada-Crespi^{46,47}, A. N. Taylor⁵², I. Tereno^{57,108}, S. Toft^{109,110}, R. Toledo-Moreo¹¹¹, F. Torradeflot^{47,46}, I. Tutusaus¹⁰¹, L. Valenziano^{5,64}, J. Valiviita^{80,81}, T. Vassallo^{66,30}, A. Veropalumbo^{27,34,33}, Y. Wang¹¹², J. Weller^{66,67}, G. Zamorani⁵, E. Zucca⁵, V. Allevalo¹, M. Ballardini^{113,114,5}, M. Bolzonella⁵, E. Bozzo⁵⁹, C. Burigana^{115,64}, R. Cabanac¹⁰¹, M. Calabrese^{116,43}, D. Di Ferdinando⁷, J. A. Escartin Vigo⁶⁷, L. Gabarra¹¹⁷, M. Huertas-Company^{51,118,119,120}, S. Matthew⁵², N. Mauri^{50,7}, A. A. Nucita^{121,122,123}, A. Pezzotta⁶⁷, M. Pöntinen⁸⁰, C. Porciani⁸⁶, V. Scottez^{91,124}, M. Tenti⁷, M. Viel^{29,30,32,31,125}, M. Wiesmann⁶⁹, Y. Akrami^{126,127}, S. Alvi¹¹³, I. T. Andika^{128,129}, S. Anselmi^{61,99,130}, M. Archidiacono^{84,85}, F. Atrio-Barandela¹³¹, D. Bertacca^{99,68,61}, M. Bethermin¹³², A. Blanchard¹⁰¹, L. Blot^{133,130}, S. Borgani^{134,29,30,31,125}, M. L. Brown²⁰, S. Bruton¹³⁵, A. Calabro⁴⁴, B. Camacho Quevedo^{105,107}, A. Cappi^{5,88}, F. Caro⁴⁴, C. S. Carvalho¹⁰⁸, T. Castro^{30,31,29,125}, F. Cogato^{4,5}, S. Conseil⁵⁴, S. Contarini⁶⁷, A. R. Cooray¹³⁶, O. Cucciati⁵, F. De Paolis^{121,122,123}, G. Desprez¹³⁷, A. Díaz-Sánchez¹³⁸, S. Di Domizio^{33,34}, J. M. Diego¹³⁹, P. Dimauro^{44,140}, A. Enia^{9,5}, Y. Fang⁶⁶, A. G. Ferrari⁷, P. G. Ferreira¹¹⁷, A. Finoguenov⁸⁰, A. Franco^{122,121,123}, K. Ganga⁸⁹, J. García-Bellido¹²⁶, T. Gasparotto³⁰, V. Gautard⁸, E. Gaztanaga^{107,105,141}, F. Giacomini⁷, F. Gianotti⁵, G. Gozaliasl^{142,80}, M. Guidi^{9,5}, C. M. Gutierrez¹⁴³, A. Hall⁵², W. G. Hartley⁵⁹, S. Hemmati¹⁴⁴, C. Hernández-Monteagudo^{98,51}, H. Hildebrandt¹⁴⁵, J. Hjorth⁹⁴, J. J. E. Kajava^{146,147}, Y. Kang⁵⁹, V. Kansal^{148,149}, D. Karagiannis^{113,150}, K. Kiiveri⁷⁸, C. C. Kirkpatrick⁷⁸, S. Kruk²⁵, M. Lattanzi¹¹⁴, J. Le Graet⁶², L. Legrand^{151,152}, M. Lembo^{113,114}, F. Lepori¹⁵³, G. Leroy^{154,87}, J. Lesgourgues⁴⁸, T. I. Liaudat¹⁵⁵, S. J. Liu⁶⁰, A. Loureiro^{156,157}, J. Macias-Perez¹⁵⁸, G. Maggio³⁰, M. Magliocchetti⁶⁰, F. Mannucci¹⁵⁹, R. Maoli^{160,44}, J. Martín-Fleitas⁹², C. J. A. P. Martins^{161,35}, L. Maurin²⁴, M. Miluzio^{25,162}, P. Monaco^{134,30,31,29}, C. Moretti^{32,125,30,29,31}, G. Morgante⁵, S. Nadathur¹⁴¹, K. Naidoo¹⁴¹, P. Natoli^{113,114}, A. Navarro-Alsina⁸⁶, S. Nesseris¹²⁶, F. Passalacqua^{99,61}, K. Paterson⁷⁵, L. Patrizii⁷, A. Pisani^{62,163}, D. Potter¹⁵³, S. Quai^{4,5}, M. Radovich⁶⁸, I. Risso¹⁶⁴, P.-F. Rocci²⁴, S. Sacquogna^{121,122,123}, M. Sahlén¹⁶⁵, E. Sarpa^{32,125,31}, A. Schneider¹⁵³, M. Schultheis⁸⁸, D. Sciotti^{44,45}, E. Sellentin^{166,42}, M. Sereno^{5,7}, L. C. Smith¹⁶⁷, J. Stadel¹⁵³, K. Tanidis¹¹⁷, C. Tao⁶², G. Testera³⁴,

R. Teyssier¹⁶³, S. Tosi^{33, 164}, A. Troja^{99, 61}, M. Tucci⁵⁹, C. Valieri⁷, A. Venhola¹⁶⁸, D. Vergani⁵, G. Vernardos^{169, 170},
G. Verza¹⁷¹, P. Vielzeuf⁶², and N. A. Walton¹⁶⁷

(Affiliations can be found after the references)

March 20, 2025

ABSTRACT

The *Euclid* mission aims to survey around 14 000 deg² of extragalactic sky, providing around 10⁵ gravitational lens images. Modelling of gravitational lenses is fundamental to estimate the total mass of the lens galaxy, along with its dark matter content. Traditional modelling of gravitational lenses is computationally intensive and requires manual input. In this paper, we use a Bayesian neural network, LENS MODelling with Neural networks (LEMON), for modelling *Euclid* gravitational lenses with a singular isothermal ellipsoid mass profile. Our method estimates key lens mass profile parameters, such as the Einstein radius, while also predicting the light parameters of foreground galaxies and their uncertainties. We validate LEMON's performance on both mock *Euclid* data sets, real Euclidised lenses observed with *Hubble* Space Telescope (hereafter HST), and real *Euclid* lenses found in the Perseus ERO field, demonstrating the ability of LEMON to predict parameters of both simulated and real lenses. Results show promising accuracy and reliability in predicting the Einstein radius, axis ratio, position angle, effective radius, Sérsic index, and lens magnitude for simulated lens galaxies. The application to real data, including the latest Quick Release 1 strong lens candidates, provides encouraging results, particularly for the Einstein radius. We also verified that LEMON has the potential to accelerate traditional modelling methods, by giving to the classical optimiser the LEMON predictions as starting points, resulting in a speed-up of up to 26 times the original time needed to model a sample of gravitational lenses, a result that would be impossible with randomly initialised guesses. This work represents a significant step towards efficient, automated gravitational lens modelling, which is crucial for handling the large data volumes expected from *Euclid*.

Key words. Gravitational lensing: strong, Methods: data analysis, Galaxies: elliptical and lenticular, cD

1. Introduction

Gravitational strong lensing is a rare astrophysical phenomenon that occurs when a massive object, such as a galaxy, bends the light coming from a background distant object. This effect is a prediction of Einstein's general relativity, and is an important tool in the study of galaxy evolution, given that a gravitational lens can magnify distant galaxies, allowing for the detailed study of structures in galaxies at high redshift (Coe et al. 2013). Moreover, the distortion of the background object gives information on the properties of the deflector. In particular, when the redshifts of source and lens are known, galaxy-galaxy strong lensing allows us to determine with extreme precision the projected total mass within the Einstein radius of the foreground galaxy, without requiring any modelling a priori. By assuming a model for the deflector mass profile, it is possible to infer more quantities related to the dark matter content of galaxies, such as the total dark matter mass and the dark matter fraction (Koopmans et al. 2006; Tortora et al. 2010; Auger et al. 2010; Sengül & Dvorkin 2022), along with other properties, such as the mass density slope and the initial mass function (Gavazzi et al. 2007; Koopmans et al. 2009; Treu et al. 2010; Sonnenfeld et al. 2013; Shajib et al. 2021); finally, through gravitational lensing, it is also possible to detect substructures of the lens galaxy (Veggetti et al. 2010). Galaxy-galaxy strong lensing is also a powerful probe of the small-scale structure of galaxy clusters (e.g., Meneghetti et al. 2020, 2022, 2023).

The *Euclid* mission will observe around 14 000 deg² of extragalactic sky from the Sun-Earth Lagrange point L2, surveying of order 10⁹ galaxies (for a description of the Euclid Wide Survey, we refer the reader to Euclid Collaboration: Scaramella et al. 2022; Euclid Collaboration: Mellier et al. 2024, while an overall description of the mission can be found in Laureijs et al. 2011).

Following *Euclid*'s launch in 2023, ESA and collaborators initiated the Early Release Observations programme (ERO, Euclid Early Release Observations 2024; Cuillandre et al. 2024a), targeting 17 astronomical objects, including galaxy clusters, nearby galaxies, globular clusters, and star-forming regions, with

the objective of demonstrating the telescope's capabilities and providing early scientific insights (Atek et al. 2024; Cuillandre et al. 2024b; Hunt et al. 2024; Kluge et al. 2024; Marleau et al. 2024; Massari et al. 2024; Saifollahi et al. 2024). Among these targets, the Perseus cluster field is especially of interest for strong lensing science, with two main projects underway: the ERO Lens Search Experiment (ELSE), where a blind visual search of galaxy-scale strong lensing systems is carried out (Acevedo Barroso et al. 2024), finding 16 lens candidates (of which five have a convincing lens model) and a parallel search of strong lenses via the use of neural networks (Pearce-Casey et al. 2024) aimed at testing their performance on a real *Euclid* field. A similar search with neural networks in the other ERO fields is carried out in Nagam et al. (2025). The first statistically relevant sample of around 500 strong lenses in *Euclid* has finally been collected with the data from the Euclid Quick Data Release 1 (Q1, Euclid Quick Release Q1 2025; Euclid Collaboration: Aussel et al. 2025), which also represents the first publicly available data set of Euclid Wide Survey (EWS)-like images, processed with the same pipeline and reaching the same depth as the final survey. Despite covering only 63.1 deg², Q1 provides a powerful testbed for *Euclid*'s lens searching capabilities, with the strong lensing discovery engine at the forefront of these efforts (Euclid Collaboration: Walmsley et al. 2025; Euclid Collaboration: Rojas et al. 2025; Euclid Collaboration: Lines et al. 2025; Euclid Collaboration: Li et al. 2025; Euclid Collaboration: Holloway et al. 2025).

High-resolution imaging, together with a large field of view, are crucial for detecting a large number of gravitational lenses. However, the substantial amount of data coming from the mission will necessarily require automated methods for both lens finding and lens modelling. Currently, convolutional neural networks (CNNs) are already used extensively in lens-finding tasks, having generally good performance (Petrillo et al. 2017, 2019a,b; Metcalf et al. 2019; Cañameras et al. 2020; Li et al. 2020; Rezaei et al. 2022; Rojas et al. 2022; Nagam et al. 2024). Instead, modelling of gravitational lenses has traditionally relied on complex and time-consuming techniques that require manual inputs, such as maximum likelihood and Markov chain Monte Carlo methods (Keeton 2016; Nightingale et al. 2021a,b;

* e-mail: valerio.busillo@inaf.it

Table 1. List of parameter ranges for the *Euclid* mock lenses.

Parameters	Range
Einstein radius R_{Ein} /arcsec	[0.51, 4.44]
Axis ratio q	[0.11, 1.00]
Position angle p.a./deg	[0, 180]
Lens effective radius $R_{\text{e, lens}}$ /arcsec	[0.05, 2.00]
Lens Sérsic index n_{lens}	[2.00, 8.00]
Lens magnitude m_{lens}	[13.88, 24.68]

Notes. Only position angle and Sérsic index are extracted from a uniform distribution. This choice has been made to avoid introducing a prior in the training of the network. All the other parameters are extracted from non-analytic, empirical distributions derived from the Flagship simulation (Euclid Collaboration: Castander et al. 2024). The coverage of the parameters in the reported intervals is thus non-uniform.

Harvey-Hawes & Wiltshire 2024). The advent of machine learning has allowed for the automation and acceleration of this process. In particular, CNNs and Bayesian neural networks (BNNs) have shown remarkable results in recovering lens parameters (Perreault Levasseur et al. 2017; Pearson et al. 2019, 2021; Schuldt et al. 2021, 2023; Gentile et al. 2023).

The main algorithm for this work is LENS MODelling with Neural networks (LEMON; Gentile et al. 2023), a BNN able to perform fast automated analysis of strong gravitational lenses. In the original work, Gentile et al. (2023) used LEMON to estimate three parameters of a strong gravitational lens modelled as a singular isothermal ellipsoid (SIE), the Einstein radius and the two components of the ellipticity, for mock HST and *Euclid* gravitational lenses. Along with the expected values, LEMON is also able to output uncertainties for each parameter.

In this work, we expand the results of Gentile et al. (2023), by predicting both mass and light parameters of the foreground galaxies in isolated galaxy-galaxy gravitational lenses, considering a single Sérsic model for the light profile and using mock *Euclid* lenses with contaminants in the image for both training and testing. We will also verify the behaviour of both uncertainty components and verify the capability of LEMON to generalise to real Euclidised HST lens images.

The paper is structured as follows. In Sect. 2 we give details on the various data sets used for the analysis. In Sect. 3 we briefly introduce the LEMON algorithm. In Sect. 4 we describe the training procedure, the metrics used to quantify the performance of LEMON, and the calibration procedure for the total uncertainty. Section 5 is dedicated to the results of the analysis on the simulated test set, while Sect. 6 shows the results associated with real Euclidised lenses and real *Euclid* lenses found in the Perseus ERO and Q1 fields. Section 7 shows how the joint use of LEMON and classical modelling methods could provide a speed up of the latter. We finally give our conclusions in Sect. 8.

2. Data

In the following, we will give details on the various data sets used for the analysis. In Sect. 2.1, the *Euclid* mock lenses used for training and testing are described. We then describe the real Euclidised lenses used for testing LEMON performance on real lenses in Sect. 2.2.

2.1. *Euclid* mock lenses

For training and performance-testing of LEMON, we have made joint use of 50 000 lenses ‘with companions’ (i.e., having con-

taminants other than the main lens in the image), each of which contributes to the projected lensing potential, and 50 000 lenses ‘without companions’. Both sets are simulated by the Strong Lensing Science Working Group of the Euclid Consortium (Metcalfe et al., in prep.). The lens images are made by simulating the *Euclid* visible instrument (VIS, Euclid Collaboration: Cropper et al. 2024) camera output, at the depth of the Euclid Wide Survey. The two samples are selected to capture the full range of environmental scenarios that may occur when observing a gravitational lens, including objects along the line of sight as well as companion or background objects surrounding the lens system. Separating the two sets allows us to also test whether the lack of training on images with companions affects the recovery of the parameters, given that the presence of companions in the image could be mistaken by the network as part of the lensing system (see App. A).

The lenses are constructed by first considering galaxies in the *Euclid* Flagship simulation (Euclid Collaboration: Castander et al. 2024), taken from a sky area of the order of 100 deg^2 , under the requirements that the galaxy chosen is brighter than the lens galaxy magnitude limit of 24 in the I_{e} band, which is the VIS imaging band, and categorised as a central galaxy. Central galaxies are galaxies that are positioned at the centres of the dark matter halos. Large halos also contain satellite galaxies, which should not produce isolated lenses like the ones we wish to model here. For each selected candidate, the apparent magnitude, effective radius, position angle, axis ratio and redshift are taken from the Flagship and converted into a surface brightness model. In general, the light model is composed of a disc and a spheroid component, but in our catalogue, only galaxies with a spheroid component are considered. This spheroid component is represented by a single Sérsic profile. The Sérsic index is uniformly distributed between 2 and 8. A mass model is then chosen by considering analytical profiles centred on each galaxy. In our catalogue, all lens mass profiles are considered to be SIE profiles.

The mass in the lens is normalised with the ratio of dark matter to stellar mass within one effective radius. The stellar mass and effective radius are taken from the Flagship simulation. The dark matter fraction within one effective radius is taken to be normally distributed with a mean of 0.6 and a standard deviation of 0.1 consistent with observations (Mukherjee et al. 2022). The axis ratio and position angle of the mass is set to those of the light.

Once the lens galaxies have been selected, a source galaxy is placed in the relative background. This increases the sample size of lenses in the data set, in order to offset the inherent rarity of ‘natural lenses’ (i.e. lenses in the Flagship simulation that naturally have a source behind them when the image is traced onto the observer plane). The redshift of the source is sampled randomly from the following distribution:

$$p(z) \propto z^\gamma e^{-z^2/z_0^2}, \quad (1)$$

where $\gamma = -0.23$ and $z_0 = 3.06$ are values found by fitting to the COSMOS 2020 Farmer catalogue I -band number counts (Weaver et al. 2022). The surface brightness is represented by between one to four Sérsic profiles. To emulate some of the complex morphologies of high-redshift sources, the number of Sérsic profiles, their relative brightnesses, and their positions are generated randomly from distributions tuned by eye. Their total brightnesses and overall sizes are based on randomly selected sources from the Hubble Ultra Deep Field (HUDF) with similar redshifts (see Meneghetti et al. 2008, 2010 for a discussion of this sample).

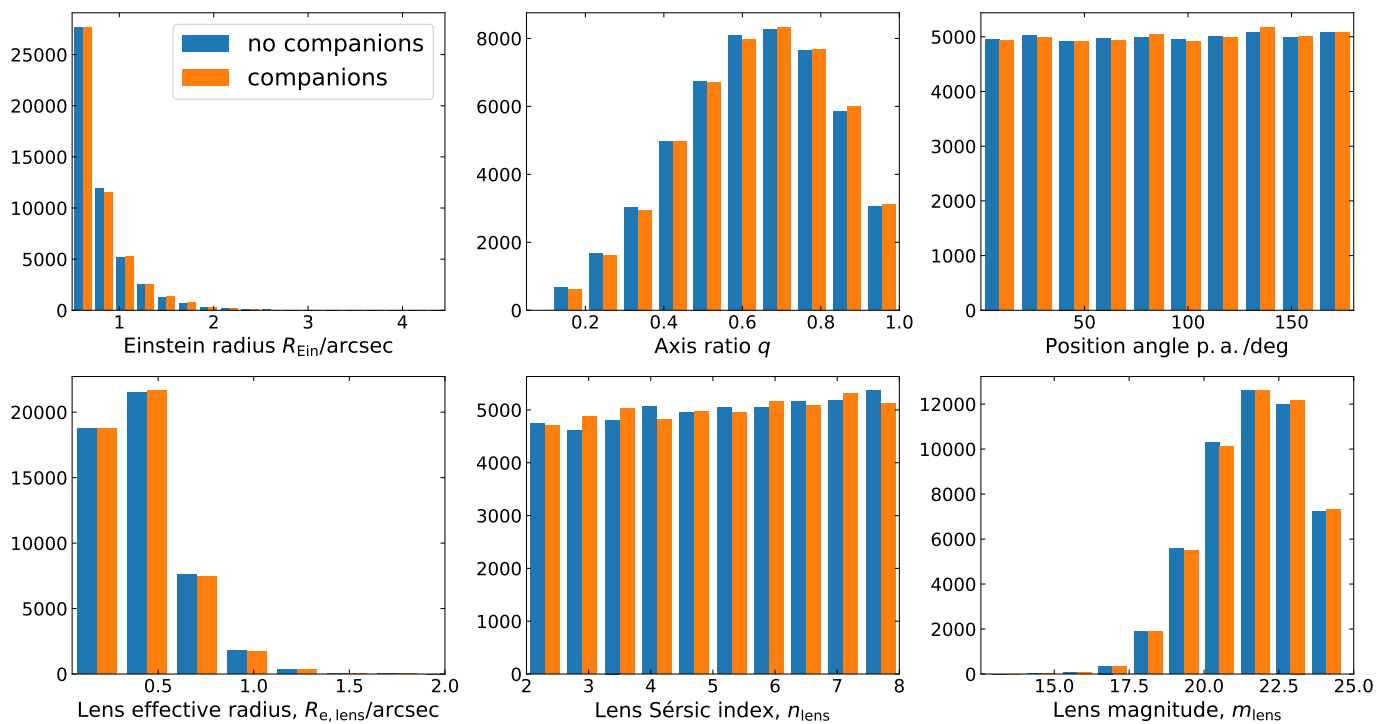


Fig. 1. Distribution of mass and light parameters for the *Euclid* mock lenses. Blue bars show the distribution of lenses without contaminants in the image, while orange bars show the distribution of lenses with contaminants.

Ray-shooting through the light cones is performed, to construct an image of the lens. The deflection caused by other objects along the line of sight is not included, so that the mass distribution remains an SIE in all cases. The lens is then rejected or accepted based on an observability criterion. This criterion seeks to filter out lenses that would not be recognisable as lenses. It combines the signal-to-noise ratio (S/N) in the lensed images, the contrast between the source and lens surface brightnesses and the morphology of the lensed source images. More details on the procedure are available in Metcalf et al. (in prep.).

A summary of the ranges of parameters for the mock lenses is listed in Table 1, with the respective distributions shown in Fig. 1. We underline the fact that, except for position angle and Sérsic index, all the other parameters are drawn from non-analytic, empirical distributions derived from the Flagship simulation, so the coverage for these parameters is not uniform. In particular, the distribution for the Einstein radius has a median equal to $0''.69$, while the one for the lens effective radius is equal to $0''.38$. An example of some mock *Euclid* lens images used for training is shown in Fig. 2.

The six parameters listed in Table 1 are the main ones that we want to predict with LEMON (the recovery of a seventh parameter, the Einstein mass, is discussed in App. B). They are listed as follows.

1. Einstein radius, in units of arcseconds, obtained via the formula

$$R_{\text{Ein}} = \frac{648\,000}{\pi} \sqrt{\frac{A_{\text{Ein}}}{\pi}}, \quad (2)$$

where A_{Ein} is the Einstein area in square radians, defined as the area of the largest critical curve, and the factor 648 000 corresponds to converting π radians into arcseconds.

2. Axis ratio, defined as $q = b/a$, where b and a are, respectively, the semi-minor and semi-major axes of the ellipsoidal distribution.
3. Position angle, defined as the clockwise angle of the semi-major axis of the ellipsoidal distribution, starting from left to top with respect to the image, in units of degrees.
4. Circularised effective radius of the lens R_e , i.e., the radius enclosing one-half of the lens galaxy light, obtained from the major axis effective radius $R_{e,\text{maj}}$ via the formula $R_e = \sqrt{q} R_{e,\text{maj}}$. We will refer to it as $R_{e,\text{lens}}$ in the following.
5. Lens Sérsic index, which regulates the slope of the surface brightness profile. It corresponds to the parameter n that appears in the Sérsic profile definition

$$I(r) = I_e \exp \left\{ -b_n \left[\left(\frac{r}{R_e} \right)^{1/n} - 1 \right] \right\}, \quad (3)$$

where $I_e = I(r = R_e)$ and b_n is a parameter, solution to the equation $\Gamma(2n) = 2\gamma(2n, b_n)$, where Γ and γ are the complete and incomplete gamma functions, respectively. We will refer to it as n_{lens} in the following.

6. Lens magnitude, defined as the apparent magnitude in the I_e band of the main lens.

It should be noted that, in these simulations, we implicitly assume that the ellipticity and orientation of the mass profile of the lens follows those of the light profile. This assumption generally holds for early-type galaxies, but outliers can be found in real scenarios, mainly due to the presence of faint discs or external galaxies that induce a substantial external shear (see e.g., Gavazzi et al. 2012). This assumption can thus lead to systematic errors in predicting lens parameters of systems where the mass does not follow the light profile, because the network tends to learn to estimate the parameters from the light distribution,

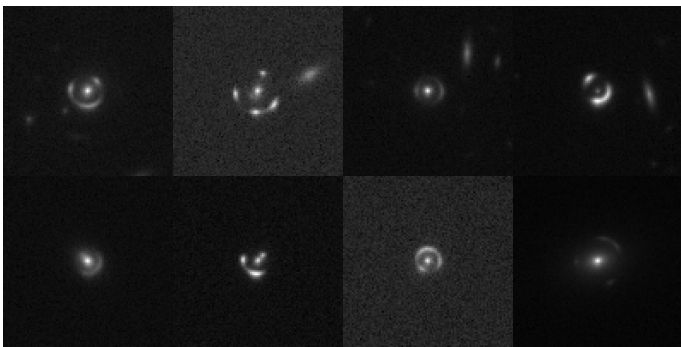


Fig. 2. $20'' \times 20''$ original VIS images of some examples of *Euclid* mock lenses used for training LEMON. *Top row:* lenses with companions in the image. *Bottom row:* lenses without companions.

rather than from the lensed image of the source, as noted in Pearson et al. (2019). In future works, we also plan to train on lenses for which this assumption does not hold, as was done in Gentile et al. (2023), albeit with more simplistic mock lenses. The original simulated images have dimensions of $20'' \times 20''$, as shown in Fig. 2, but during the training of LEMON we create $10'' \times 10''$ cutouts of these images, centred on the lenses, in order to better see the lens features.

2.2. Euclidised lenses

In addition to the set of simulated images, we test the performance of LEMON using a sample of known strong gravitational lenses. These lenses are observed during several strong lensing surveys with HST or serendipitously discovered in the HST archive. Section 6.1 gives more details on the data set. We use the code HST2EUCLID (Bergamini et al., in prep.) to Euclidise the HST images, mimicking *Euclid* observations of these sources at the same depth and resolution of the EWS in the I_E band.

We summarise here the procedure implemented in HST2EUCLID. For more details, we refer the reader to Bergamini et al. (in prep.). First, we convert the pixel values of the HST images from units of electrons per second ($e s^{-1}$) to physical flux densities ($\text{erg s}^{-1} \text{cm}^{-2} \text{Hz}^{-1}$). We perform this operation for all available HST images in photometric bands overlapping with the I_E passband. For the lenses in the data set used in this paper, we use only HST observations with the Advanced Camera for Surveys (ACS) in the F814W band.

In the second step, we account for the *Euclid* PSF. Since the input images are already convolved with the HST PSF, we do not convolve them directly with the *Euclid* PSF model. Instead, we create a convolution kernel that matches the HST to the *Euclid* PSF. Since we could not measure the PSF for each HST lens, we use a model for the ACS observations in the F814W band computed with the software TinyTim.¹ The matched kernel for each pair of HST and *Euclid* PSFs is computed with the Python function `create_matching_kernel` of the Photutils package² (Bradley et al. 2023). We then re-bin the images from the HST pixel grid to the correct *Euclid* pixel scale. The resulting images have pixel scales of 100 mas px^{-1} in the I_E band. The re-binned images, expressed in units of physical flux densities, are then converted into units of electrons per second using the *Euclid* zero point.

¹ <https://www.stsci.edu/hst/instrumentation/focus-and-pointing/focus/tiny-tim-hst-psf-modeling>

² <https://photutils.readthedocs.io/en/stable>

Finally, we add Poisson photon noise. To accomplish this task, we assume that the noise in the input HST background subtracted images is negligible compared to the noise in the *Euclid* observations. This approximation is supported by the significantly greater depth of the HST observations compared with the *Euclid* images. We adjust the noise level to achieve the nominal S/N of 10 for an extended source of magnitude 24.5 within an aperture of $0''.65$ radius expected for the EWS (Euclid Collaboration: Scaramella et al. 2022).

3. Introduction to LEMON

LEMON (Gentile et al. 2023) is a BNN (Charnock et al. 2020), a machine-learning algorithm that employs the feature-recognition capabilities of a CNN to predict model parameters of a gravitational lens, using Bayesian statistics to estimate the respective uncertainties. The key point of LEMON is its ability, by using BNNs, to estimate the two main sources of uncertainty in machine-learning inference applications, namely epistemic uncertainty and aleatoric uncertainty.

- Aleatoric uncertainty: also known as statistical uncertainty, is associated with the intrinsic quality of the data analysed by the algorithm. The most common sources of aleatoric uncertainty are a low S/N, corruptions in the images (e.g., masked regions) and source blending. This kind of uncertainty cannot be reduced with training, because it depends on the quality of the image being analysed.
- Epistemic uncertainty: also known as systematic uncertainty, it is caused by a lack of knowledge about the best model. It refers to the ignorance of the machine-learning algorithm about a certain region of the parameter space, and hence to the state of the machine rather than to the state of the images. This kind of uncertainty can be reduced with a higher completeness of the training set.

The aleatoric uncertainty for a certain image is given as an output by LEMON, together with the predicted parameter value (for details on how the aleatoric uncertainty is predicted by LEMON, refer to Gentile et al. 2023). The epistemic uncertainty for an image can be obtained thanks to the dropout layers of LEMON: by randomly switching off some connections between the neurons of the neural network, predicting repeatedly the parameters associated to a single image is equivalent to sampling from the posterior probability of the parameters. The epistemic uncertainty can then be evaluated by measuring the standard deviation of this sampled distribution.

The total uncertainty for a generic parameter p can be obtained via the following procedure (Gentile et al. 2023). For each image, LEMON predicts the mean value, \bar{p} , and the aleatoric uncertainty, σ_A , for p . A value p_i is then sampled from a Gaussian distribution centred on \bar{p} with a standard deviation equal to σ_A . This is repeated N times (we used $N = 50$ to optimise for speed), sampling the posterior distribution of the parameter p . Finally, we compute the standard deviation of the distribution associated with the extractions of p_i , obtaining the total uncertainty.

LEMON employs the ResNet architecture (He et al. 2015), a deep residual network known for its success on computer vision tasks (Russakovsky et al. 2015). The architecture of LEMON is composed of: convolutional layers, used for feature extraction; dropout layers, to facilitate Bayesian uncertainty estimation through Monte Carlo sampling; finally, a fully connected layer made by $2N_{\text{param}}$ nodes, with N_{param} number of parameters

estimated by the network. A corresponding number of aleatoric uncertainties is estimated through the minimisation of a Gaussian log-likelihood loss function, with an additional regularisation term in order to prevent overly large or small variance estimates. Technical details on the implementation can be found in [Gentile et al. \(2023\)](#).

4. Methods

In this section, we will first describe the training procedure for LEMON in Sect. 4.1. Section 4.2 is dedicated to the description of the metrics that we used to evaluate the performance of LEMON. Finally, Sect. 4.3 is dedicated to discussing the calibration procedure for the total uncertainty.

4.1. Training the network

We prepare the training of LEMON by taking the full sample of 100 000 mock *Euclid* lenses, both with and without companions in the image, and splitting it into a training set formed by 80 000 lenses (equally split between companions and non-companions), a validation set and a test set formed by 10 000 lenses each (equally split as before). We shuffle the three sets to avoid possible biases during learning. Differently from [Gentile et al. \(2023\)](#), we use the ResNet-50 architecture ([He et al. 2015](#)) when implementing LEMON. The increased number of layers with respect to ResNet-34 should improve the accuracy in the recovery of the parameters. Before feeding the images into LEMON, we apply a preprocessing step where pixel values are first rescaled to the range [0,1], and then transformed using a square root scaling to enhance the visibility of low-intensity features.

Training is performed via stochastic gradient descent, with a batch size of 64 images. For the optimiser, we used ADAM ([Kingma & Ba 2015](#)), with a starting learning rate of 10^{-4} . To prevent overfitting, we used both the ReduceLRonPlateau and EarlyStopping callbacks of the keras Python library. The former reduces the learning rate of the optimiser when no improvement is seen for a given number of epochs, while the latter stops the training when the validation loss stops decreasing. Dropout layers, needed for estimating the epistemic uncertainty, are employed at both training and testing time, with a drop rate of 0.05.

We performed the training via the tensorflow Python library ([Abadi et al. 2015](#)), using a single Nvidia RTX 4080 graphics processing unit (GPU). The whole training procedure required 15 hours and 30 minutes, with a total of 70 epochs.

4.2. Metrics

To evaluate the performance of LEMON in recovering the lens parameters, we make use of various statistical estimators.

- Bias, defined as

$$\mu(\hat{\mathbf{y}}, \mathbf{y}) := \text{median}(\hat{\mathbf{y}} - \mathbf{y}), \quad (4)$$

where $\hat{\mathbf{y}}$ and \mathbf{y} are the arrays of the predicted and the true parameter values, respectively.³ This is an indicator of the accuracy of the prediction: higher bias values indicate a systematic overestimation of the predictions, and vice versa for lower bias values.

³ A single predicted value \hat{y}_i is the mean of the distribution of the \mathcal{N} parameter extractions p_j described in Sect. 3.

- Discrepancy distribution scatter: the scatter of the discrepancy distribution is obtained from the 16th and 84th percentiles of the discrepancy distribution via the following definitions:

$$\sigma^- := \text{median}(\hat{\mathbf{y}} - \mathbf{y}) - \text{percentile}_{16\text{th}}(\hat{\mathbf{y}} - \mathbf{y}), \quad (5)$$

$$\sigma^+ := \text{percentile}_{84\text{th}}(\hat{\mathbf{y}} - \mathbf{y}) - \text{median}(\hat{\mathbf{y}} - \mathbf{y}). \quad (6)$$

Bigger values of these metrics indicate higher scatter from the ideal $\hat{y} = y$ relation. Since they are obtained from the percentiles, these quantities are robust estimators of the scatter.

- Root mean square error (RMSE), defined as

$$\text{RMSE} := \sqrt{\frac{1}{N} \sum_{i=1}^N (\hat{y}_i - y_i)^2}, \quad (7)$$

where \hat{y}_i and y_i are the generic components of the $\hat{\mathbf{y}}$ and \mathbf{y} arrays, respectively, which have length N . This metric is a measure of predictive power: a value of zero indicates a perfect fit to the true parameter values.

- Mean absolute error (MAE), defined as

$$\text{MAE} := \frac{1}{N} \sum_{i=1}^N |\hat{y}_i - y_i|. \quad (8)$$

This metric is similar, but not equivalent to RMSE. It is the average absolute vertical distance between each point (y_i, \hat{y}_i) and the ideal $\hat{y} = y$ relation.

- Normalised median absolute deviation (NMAD), defined as

$$\text{NMAD} := 1.48 \text{median}[(\hat{\mathbf{y}} - \mathbf{y}) - \text{median}(\hat{\mathbf{y}} - \mathbf{y})]. \quad (9)$$

The NMAD is roughly analogous to the standard deviation ($\sigma \approx \kappa \text{MAD}$, where MAD is the median absolute deviation and κ is a constant scale factor, which is approximately equal to 1.48 for normally distributed data). An advantage of the NMAD metric is that it is a non-parametric estimator, which is robust to outliers.

- Coefficient of determination, defined as

$$R^2 := 1 - \frac{\sum_{i=1}^N (\hat{y}_i - y_i)^2}{\sum_{i=1}^N (y_i - \bar{y})^2}, \quad (10)$$

where

$$\bar{y} = \frac{1}{N} \sum_{i=1}^N y_i \quad (11)$$

is the mean value of the true parameter over all the lenses. This metric provides a measure of how well the parameters are predicted by LEMON. Given a fixed parameter, if it is perfectly predicted by the network, $\hat{y}_i = y_i$ for all the points of the data set, and thus $R^2 = 1$. A baseline network, which always outputs the mean value of the true parameter (i.e., $\hat{y}_i = \bar{y}$), will produce $R^2 = 0$. If the network performs worse than the baseline model (i.e., the mean of the data provides a better fit than the predicted values), the values of R^2 will be negative.⁴

⁴ Notice that the coefficient of determination is not the square of a quantity R , and therefore can also assume negative values.

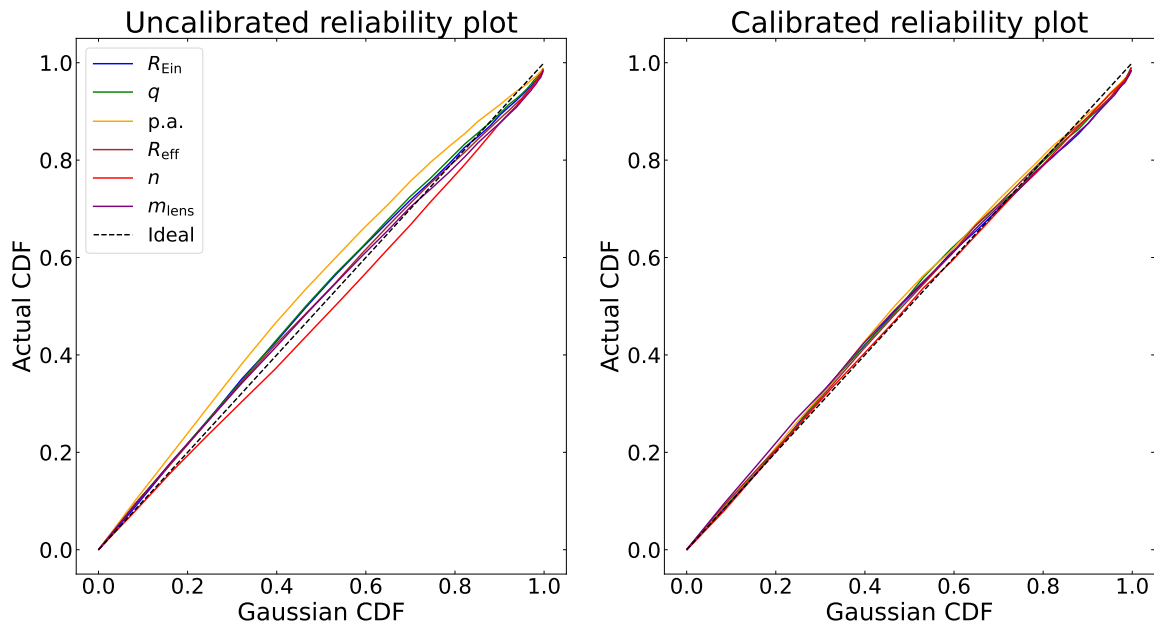


Fig. 3. Reliability plots for the parameters predicted by LEMON. *Left*: trends before the calibration procedure. *Right*: trends after the calibration procedure.

Table 2. Rescaling factors used for the calibration procedure of each parameter predicted by LEMON.

Parameter	Scaling factor
Einstein radius $R_{\text{Ein}}/\text{arcsec}$	0.99
Axis ratio q	0.97
Position angle p.a./deg	0.91
Lens effective radius $R_{e, \text{lens}}/\text{arcsec}$	1.01
Lens Sérsic index n_{lens}	1.07
Lens magnitude m_{lens}	1.02

4.3. Calibration procedure

Uncertainties produced by BNNs are known to be affected by a systematic over- or under-estimation of the confidence intervals (Guo et al. 2017). Therefore, a calibration procedure for the uncertainties is required. Following Gentile et al. (2023), we implement the Platt-scaling method (Kull et al. 2017), which consists in rescaling the predicted total uncertainty of a given parameter by a factor s : $\sigma \rightarrow s\sigma$, in order to match the empirical cumulative distribution function (CDF) with the CDF of a Gaussian distribution.

To obtain the scaling factors, we first proceed by splitting the validation set into 70% for the calibration training set and 30% for the calibration test set. We then build the uncalibrated reliability plot, by putting on the x -axis the values extracted from the CDF of a Gaussian distribution and on the y -axis the respective values extracted from the actual CDF. We fit the resulting trend with a β -function, and find the Platt-scaling factor, s , by minimising the difference between the β -function and the bisector of the reliability plot. This is done for each parameter, obtaining the values reported in Table 2.

Figure 3 shows the uncalibrated reliability plot for each parameter in the left panel, and the calibrated reliability plot on the right panel. We can see from the figure that the calibration

procedure has its biggest effect on the position angle and Sérsic index uncertainties, which were previously systematically overestimated and underestimated, respectively.

5. Results for the test set

In the following, we will present the results of the analysis on the mock *Euclid* test set. In Sect. 5.1, we show the recovery of the parameters, along with the trends for the bias and the NMAD for each parameter. In Sect. 5.2, we analyse the behaviour of the uncertainties for each parameter. In App. A, we show the degradation in performance if one uses lenses without companions for training to predict parameters of lenses with companions in the cutouts.

5.1. Recovery of parameters for *Euclid* mock lenses

Figure 4 shows the recovery of the parameters of the *Euclid* mock lenses for the test set, for both the mass and light profiles, with the bottom two rows of each parameter showing the bias and NMAD metrics in sequential bins. Overall, the recovery of the parameters for the simulated *Euclid* lenses of the test set is good, as shown for example in Fig. 5, where we compare the Einstein radius predictions for a random selection of 20 test set lenses with the corresponding ground truth.

The Einstein radius is recovered well up to values of $2''0$, where the metrics start to diverge, due to a skewed prior towards zero for the Einstein radius parameter, as we can see from Fig. 4a, where we observe a sharp decrease in the bias and a corresponding increase in NMAD values. The axis ratio is well recovered over all the range of the parameter, with a practically constant scatter, as shown by the NMAD in Fig. 4b. The position angle is also well recovered, but it shows the typical loss of recovery around p.a. = 0° and p.a. = 180° , shown as a divergence of the bias from the expected null value and an increase in NMAD values around the edges, due to the fact that

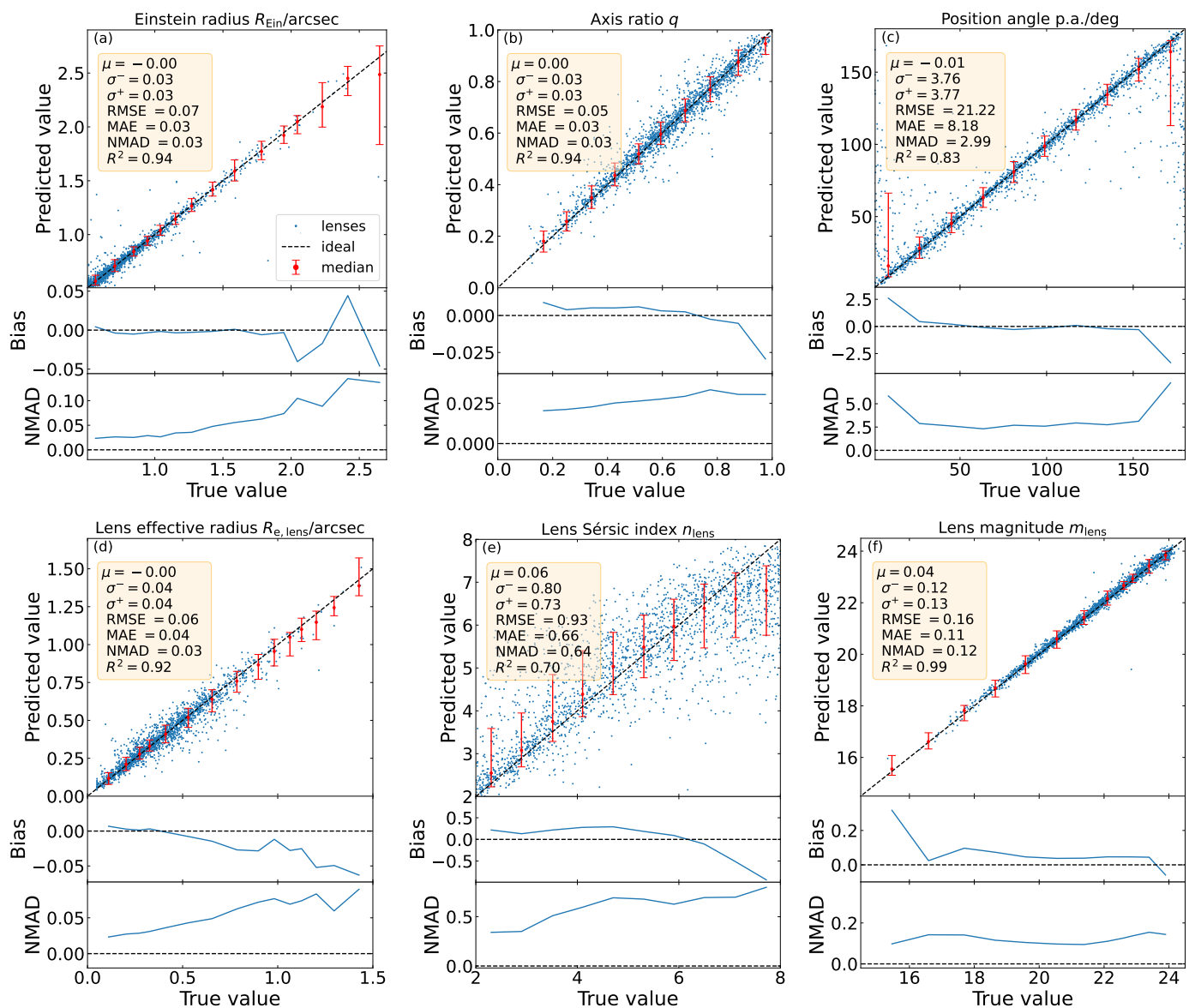


Fig. 4. Recovery plot of the parameters of *Euclid* mock lenses, showing how well the predicted model parameters from LEMON (y coordinate) reproduce the corresponding true value (x coordinate), for each lens of the test set (blue points). The ideal recovery line is shown as a dashed black line. The median trend of the scatter plots, along with the respective scatters associated with the 16th and 84th percentiles, are shown as red points and bars, respectively. For each panel, we also report the respective cumulative metrics. The bottom two rows of each parameter show the bias and the NMAD, respectively, as defined in Sect. 4.2, as a function of the true value of the parameters estimated by LEMON. For clarity, we have plotted only 2000 random points from the test set.

these two values are degenerate and the network cannot distinguish between the two configurations. The effective radius shows the same behaviour as the Einstein radius, being slightly underestimated at values of $R_e \gtrsim 0''.50$. This is also expected from the skewed prior for the effective radius parameter. It should be noted from Fig. 4d, however, that the lowest bias value is around $-0''.06$, which is negligible. The worst recovered parameter is the Sérsic index, which shows the lowest value of the coefficient of determination, $R^2 = 0.70$, and a very large scatter, which increases for an increasing value of n_{lens} . The median trend also shows a deviation from the linear trend for high values of the Sérsic index, as shown from the bias trend in Fig. 4e. This is however in agreement with GALNET, a CNN that has shown remarkable abilities in recovering the light parameters of simulated

and real KiDS galaxies⁵ (Li et al. 2022). There is finally a constant slight overprediction for the magnitude, of order $\mu \simeq 10^{-2}$, which increases for brighter lenses ($m_{\text{lens}} \lesssim 18$). This can be seen as a sharp increase in the bias in Fig. 4f, with a corresponding increase in the NMAD value. This effect is most likely due to the very high difference between the flux of the lens and the flux of the source images, not allowing the network to find the correct magnitude.

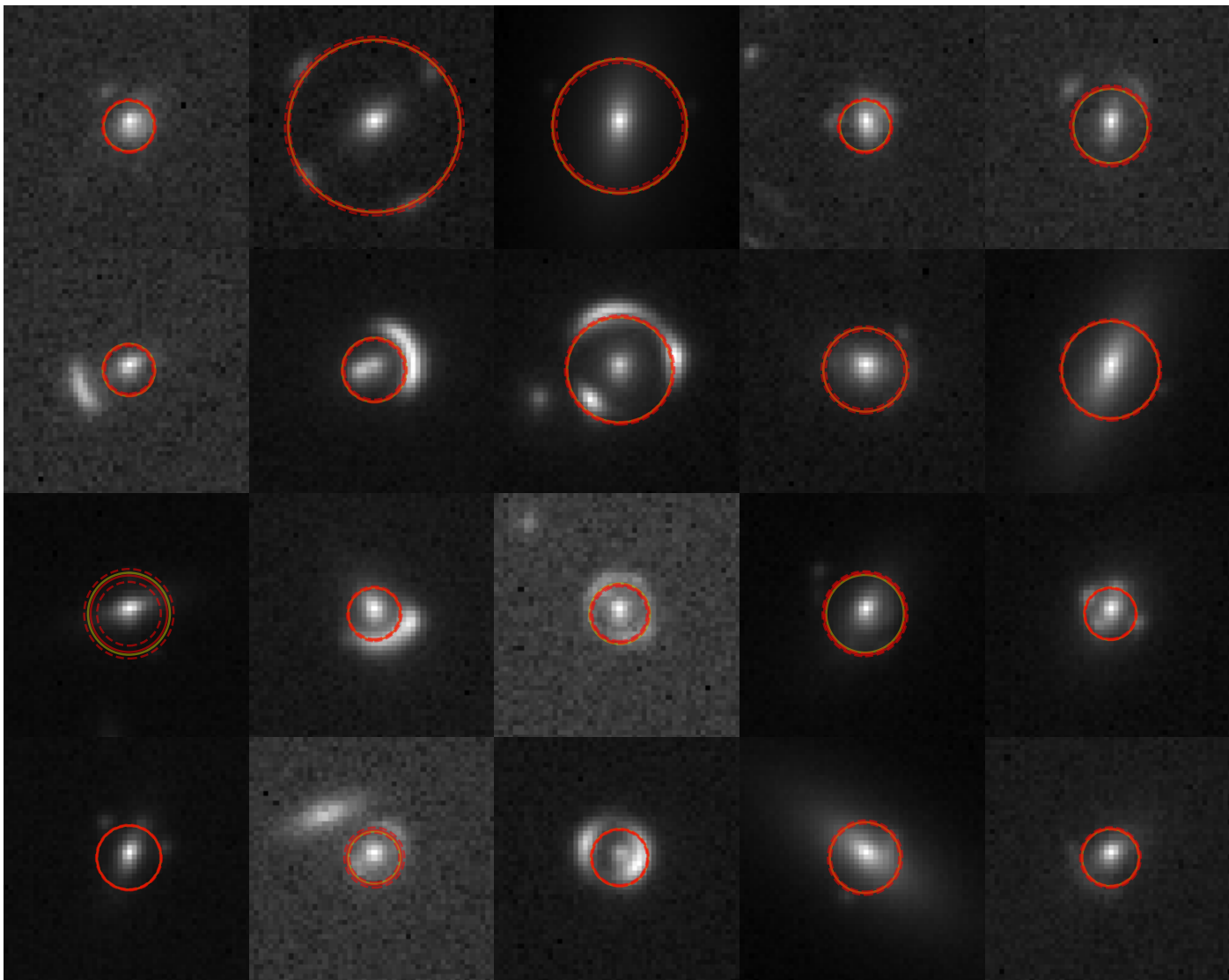


Fig. 5. Random selection of 20 $10'' \times 10''$ cutouts of simulated lenses taken from the test set. Red circles show the best predictions for the Einstein radius from LEMON, with corresponding 16th and 84th percentiles shown with dashed red circles. Yellow circles show the true values for the Einstein radii. Predictions and true values are very similar, so in some cases the corresponding circles completely overlap.

5.2. Behaviour of LEMON uncertainties

Figure 6 shows the trends for the calibrated total relative uncertainties for all predicted parameters (except for the magnitude, where we consider the absolute uncertainty, given that it is intrinsically a logarithmic quantity). From the figure, we can see that the scatter on the Einstein radius relative uncertainty increases at low radius values. This is probably an effect related to the fact that arcs and rings in strong lenses with smaller Einstein radii become embedded in the lens light, and thus the recovery becomes more uncertain. Other sources of uncertainty include the finite source size and, to a lesser extent, the PSF smearing. Regarding the axis ratio, the scatter increases for low q values. Checking the absolute uncertainty shows that the error is constant, thus this effect is mainly due to the fact that the denominator in the definition of relative uncertainty is approaching zero. Overall, the uncertainty on this parameter is consistently low. The same can be said for the position angle, except for values around p.a. = 0°

⁵ The algorithm makes use of the local PSF to enhance the predicting abilities of the network, but does not offer insights on the uncertainty associated to the predictions.

and p.a. = 180° , due to the degeneracy explained in Sect. 5.1. The trends for the lens effective radius is similar to the one for the Einstein radius, probably due to resolution, pixel scale, and PSF effects at low radii, other than S/N and magnitude, given the correlation of the effective radius with the latter. The scatter of the Sérsic index is systematically high for all values of n_{lens} , probably due to low S/N lowering the precision of LEMON in recovering this parameter. The relative uncertainty for this parameter, however, mainly remains below 40%. Finally, for both low and high values of lens magnitude, we find that the relative uncertainty increases, with a higher increase for fainter lenses. This can be explained by the fact that, for low values of magnitude, the lens is too bright and the exact value of magnitude can become difficult to estimate. For high values of magnitude, instead, the lens is too faint, and features become difficult to recognise.

We also verified whether the uncertainty on the parameters changes as a function of both S/N and number of companions in the test set images. For the S/N, we use the parameter $n_{\text{pix, source}}$, which gives the number of pixels in the lensed source image above 4σ . Results show that the uncertainty for the Einstein radius slightly decreases with an increasing value of $n_{\text{pix, source}}$,

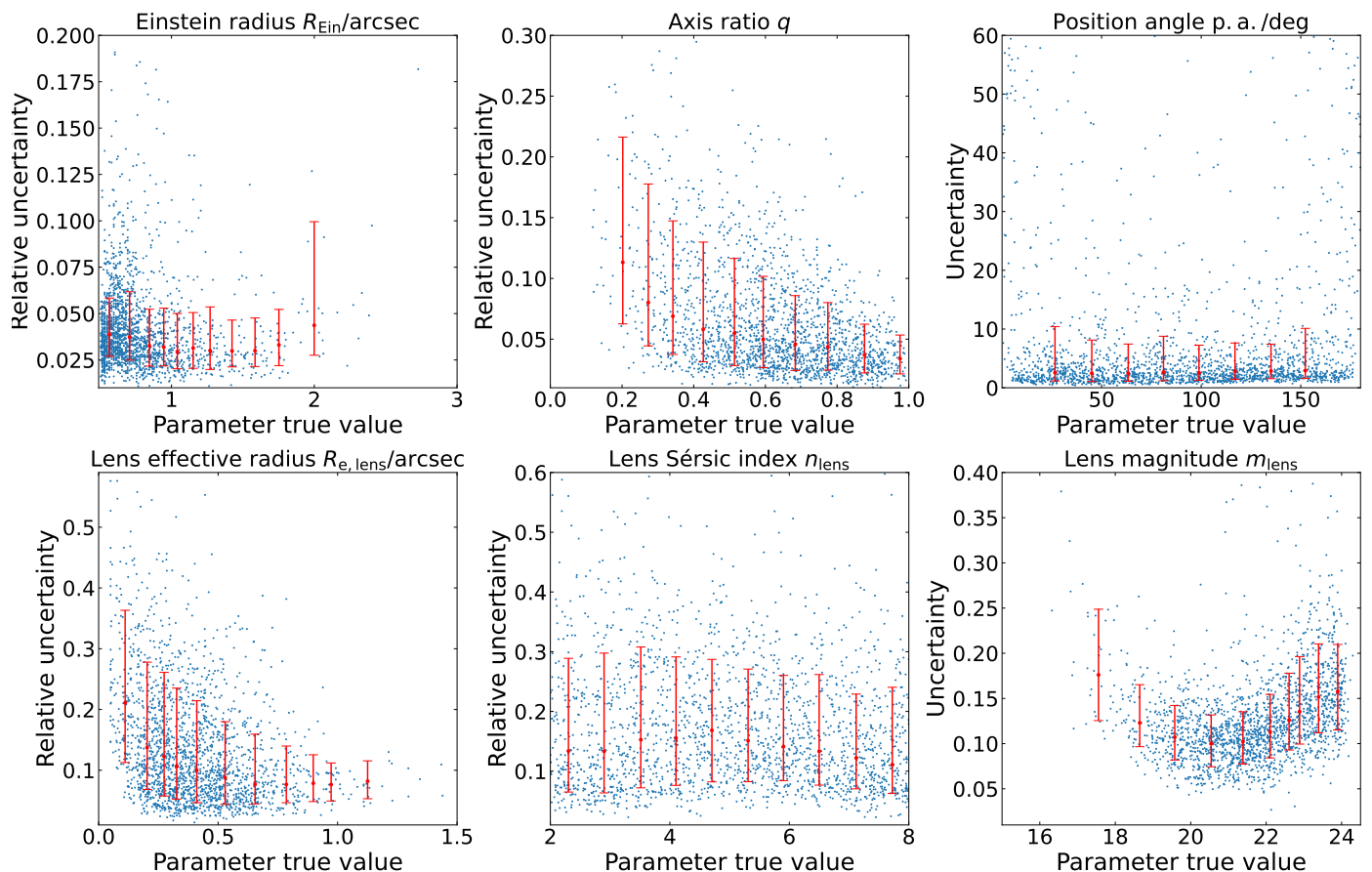


Fig. 6. Calibrated relative uncertainty as a function of the true value of the lens parameters. For the position angle and lens magnitude, we consider the absolute uncertainty. For clarity, we plotted only 2000 random points. The median trends of the scatter plots, along with the respective scatters associated with the 16th and 84th percentiles, are shown as red points and bars, respectively.

while the uncertainties for all the other parameters slightly increase. There is, instead, no correlation between uncertainty and number of companions in the images.

The behaviour of the aleatoric and epistemic relative uncertainties associated to the test set is shown in Fig. 7, where the estimated uncertainties of both types are plotted for each lens as a function of the true values of the respective parameters. From the figure, we see that the epistemic uncertainties are systematically lower than the corresponding aleatoric uncertainties. This is the expected behaviour: if the training set correctly spans all the parameter space, the epistemic uncertainties should be as close to zero as possible.

6. Results for real lenses

6.1. LEMON applied to Euclidised lenses

We now apply LEMON to a sub-sample of real Euclidised lenses described in Sect. 2.2. This sub-sample is formed by four different main catalogues, from which the ground truth values have been taken (where available).

- A sample of 29 Sloan Lens Advanced Camera for Surveys (SLACS) catalogue systems, described in Bolton et al. (2008) and Auger et al. (2009).
- The sample of 13 early-type/early-type lens systems (EELs) presented in Oldham et al. (2017).
- A sample of five lenses found in the COSMOS survey (Scoville et al. 2007), detailed in Faure et al. (2008).

- A sample of 13 lenses taken from those found by visually inspecting the whole imaging data taken with the ACS through the F814W filter up to the 31st of August 2011 (Pawase et al. 2014). Notice that the Einstein radius for these lenses is not reported, and as such we used the radius of the arc (in arcseconds) as a substitute.

All of the Euclidised lenses used in this work have been spectroscopically confirmed. The recovery plot for these lenses is shown in Fig. 8, while the cumulative metrics for each parameter are reported in Table 3. A panel with some of the lenses from each catalogue is shown in Fig. 9.

From the table, we can see that the recovery of the Einstein radius shows a systematic overestimation of the parameter, with a cumulative bias of $\mu = 0''.17$. A reason for this bias could be the fact that many of these lenses are asymmetric, with the counterimage not visible, or a low S/N for the arcs, as can be seen in some of the lenses presented in Fig. 9. Both of these effects are a result of the Euclidization procedure, which employs a worse PSF and pixel scale with respect to HST. As a result, a faint arc or a counterimage could become invisible due to the degradation of the image. Axis ratio and position angle are recovered with discrete accuracy, showing values of cumulative bias equal to $\mu = 0.02$ and $\mu = -1.93$, respectively. The recovery of the effective radius is good, having a slight bias of $0''.19$ and an NMAD of $0''.23$. Finally, due to a low number of points available for the Sérsic index parameter, we cannot draw any relevant conclusions on its recovery.

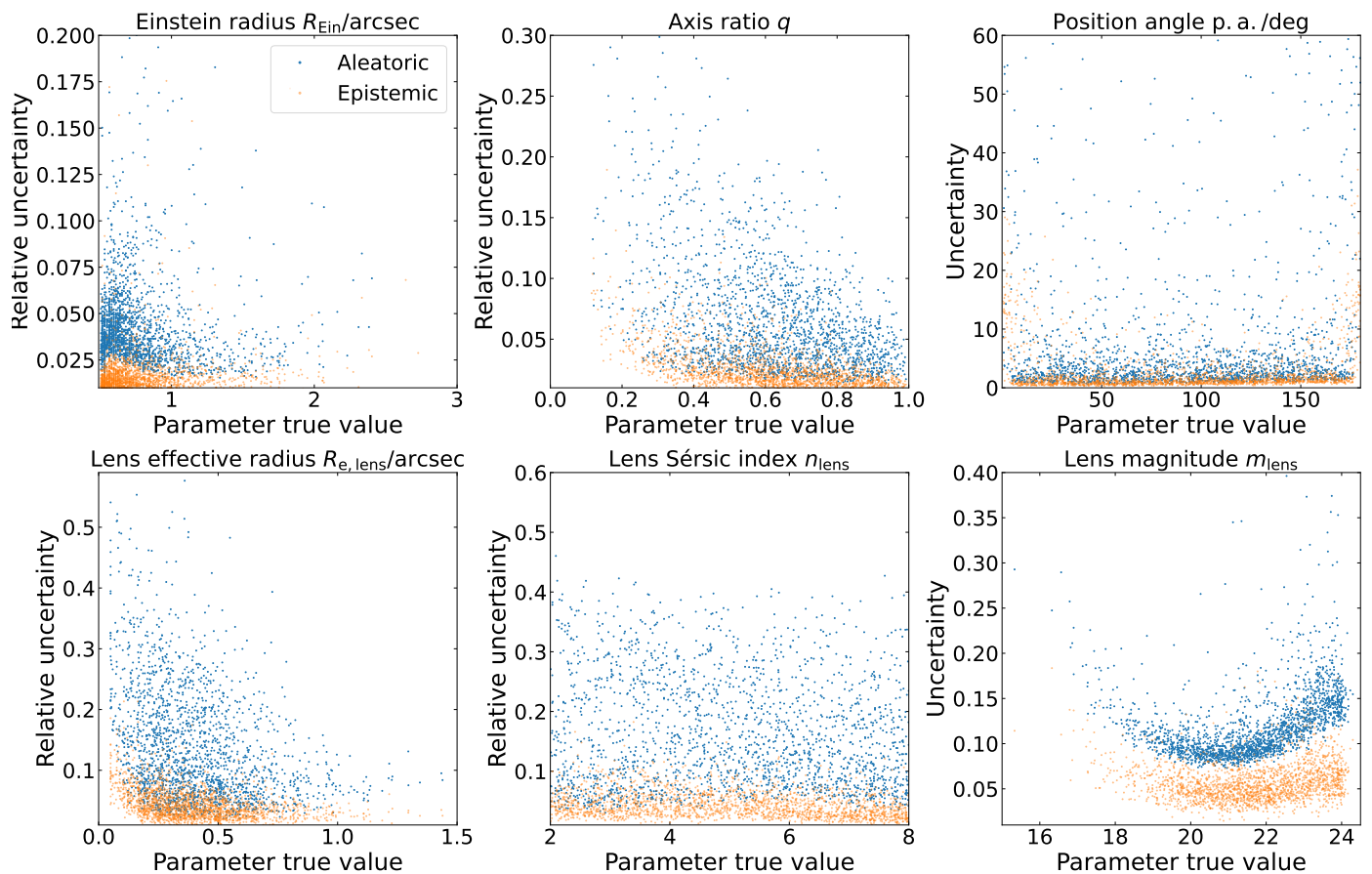


Fig. 7. Trends of aleatoric (blue) and epistemic (orange) relative uncertainties as a function of the true value of the lens parameters. For the position angle and lens magnitude, we consider the absolute uncertainties. For clarity, we plotted only 2000 random points from the test set.

Table 3. Cumulative metrics associated to the recovery of the parameters of the Euclidised lenses.

Metrics	R_{Ein} (arcsec)	q	p.a. ($^{\circ}$)	$R_{e, \text{lens}}$ (arcsec)	n_{lens}
Bias (μ)	0.17 (0.14)	0.02 (0.01)	-1.93 (-2.36)	0.19 (0.22)	0.47 (0.96)
Lower discr. scatter (σ^-)	0.19 (0.12)	0.10 (0.08)	11.18 (11.01)	0.51 (0.53)	1.30 (1.48)
Upper discr. scatter (σ^+)	0.39 (0.24)	0.10 (0.12)	12.77 (9.60)	0.13 (0.11)	2.57 (2.52)
RMSE	0.63 (0.48)	0.11 (0.11)	32.47 (26.51)	0.38 (0.39)	1.94 (2.13)
MAE	0.42 (0.30)	0.09 (0.08)	18.10 (13.55)	0.32 (0.32)	1.46 (1.63)
NMAD	0.23 (0.14)	0.11 (0.11)	9.11 (10.13)	0.23 (0.22)	1.54 (2.06)
Coefficient of determination (R^2)	-0.03 (0.91)	0.51 (0.76)	0.57 (0.98)	0.49 (0.53)	-0.16 (-0.02)

Notes. Values in parentheses correspond to the values of the cumulative metrics on the subset of lenses with predicted low uncertainty on the Einstein radius ($\sigma_{R_{\text{Ein}}} \leq 0.5''$).

In order to try and reduce the noise induced on the cumulative metrics by lenses with low S/N, we re-evaluated them by removing all lenses having predicted uncertainty on the Einstein radius bigger than $0''.5$. Results are shown in the parentheses of Table 3. We can see that the metrics of Einstein radius, axis ratio, and position angle improve substantially, with the values of R^2 reaching values of up to 0.98 for the latter. There is, however, no improvement on the metrics of the other parameters. When we remove uncertain effective radii or Sérsic indices, though, the statistical indicators for these parameters do not improve significantly.

To analyse the behaviour of LEMON with respect to the Euclidised lenses, we first evaluated both the aleatoric and epistemic components of the uncertainties for these lenses, obtaining values of epistemic uncertainties much lower than the aleatoric

ones (e.g., the maximum epistemic uncertainty for the Einstein radius is at most $0''.25$, while the corresponding maximum aleatoric uncertainty is $1''.35$), in agreement with the results for the test set. These values, however, are much higher than the components of the uncertainties for the test set (e.g., the maximum aleatoric uncertainty for the Einstein radius for the test set is $0''.20$, which is of the order of the maximum epistemic uncertainty for the Euclidised lenses set). This means that the Euclidised lenses exhibit more noise than the mock *Euclid* ones, with features that often get lost in the resolution reduction procedure, and as such we expect a loss of performance on these lenses.

We also checked the distribution of the Einstein and effective radii as a function of the lens redshifts, as can be seen in Fig. 10. From these, we can see that the parameters for the Eu-

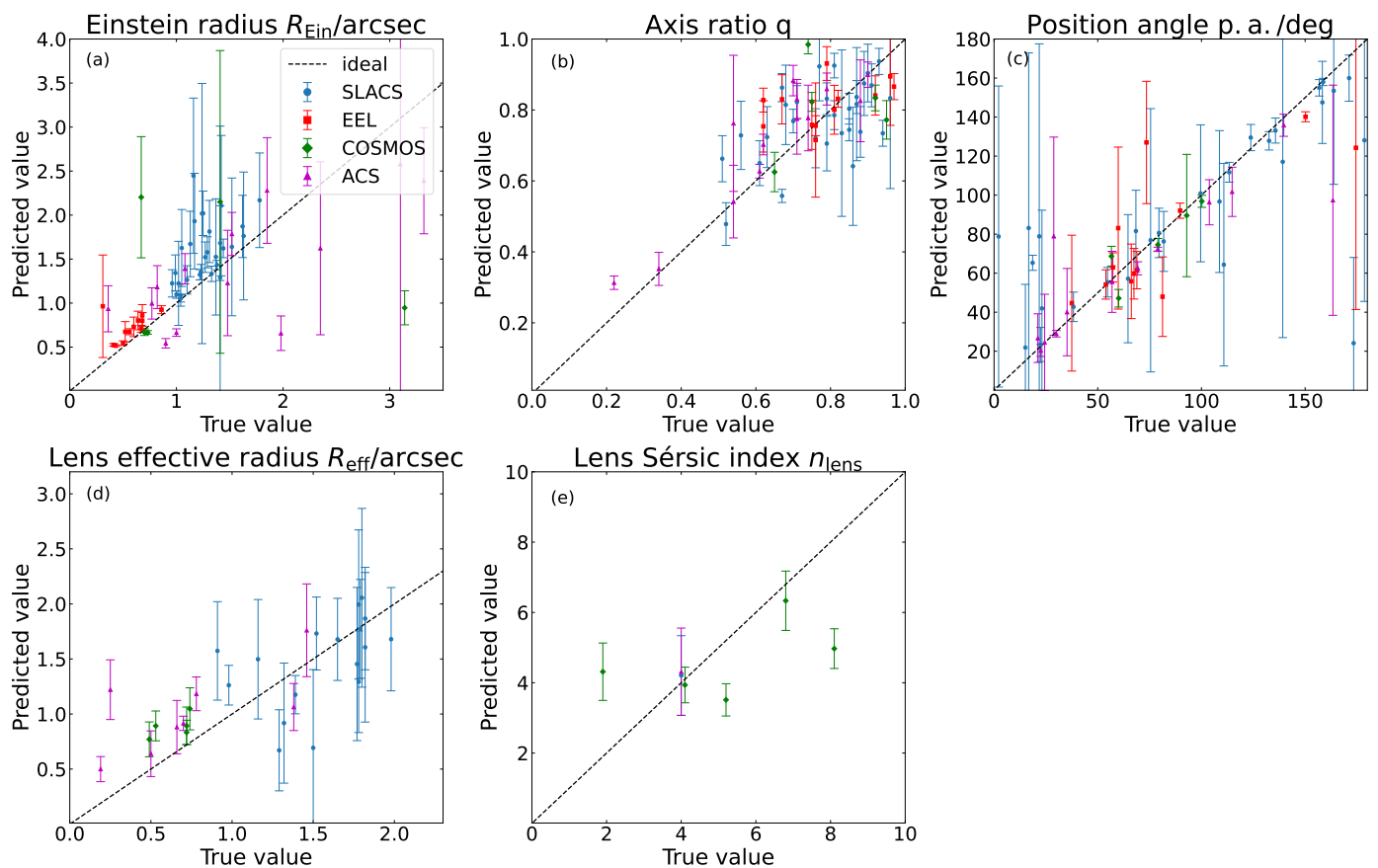


Fig. 8. Recovery plot for the parameters of the Euclised lenses, showing how well the predicted model parameters from LEMON (y coordinate) reproduce the corresponding true value (x coordinate), for each lens. The ideal recovery line is shown as a dashed black line. The SLACS and ACS best values for the Sérsic indexes are evaluated as the median of the predictions against the value for a De Vaucouleurs profile ($n_{\text{lens}} = 4$), with uncertainty given by the NMAD of the predictions. Lenses in panel (d) with true values bigger than $2''$ have been removed due to being outside the training space of LEMON.

clidised lenses are often on the edge of the training-set distribution, if not completely outside it. This could influence negatively the recovery of these parameters, given that the network is not trained to recognise this region of the parameter space. In particular, in panel (d) of Fig. 8, we removed lenses with true effective radii larger than $2''$, since they fall outside the training sample of LEMON, thus making their predicted values unreliable extrapolations. Furthermore, the true estimates of the effective radii cannot always be compared homogeneously with the predictions, as SLACS and ACS lenses are modelled with a fixed De Vaucouleurs profile (i.e., $n_{\text{lens}} = 4$), while LEMON considers Sérsic profiles with variable values of n_{lens} . Additionally, the fitting process should ideally remove the arc to obtain an accurate estimate; otherwise, the Sérsic fit may overestimate the radius due to bumps in the surface brightness profile. In future works, we will expand the distribution of the training set to cover more of the parameter space, and check if the recovery of these parameters improves.

6.2. LEMON applied to real Euclid ERO lenses

We also applied LEMON to real *Euclid* lenses found in the Perseus ERO field and modelled in Acevedo Barroso et al. (2024). The modelling has been performed with the `pronto` software (Vegetti & Koopmans 2009; Rybak et al. 2015a,b; Rizzo et al. 2018; Ritondale et al. 2019; Powell et al. 2021), with the

lens mass distribution modelled by an SIE and the light distribution modelled as a composite of three Sérsic profiles. The surface brightness distribution of the source is reconstructed using a pixelated, free-form approach. Regularisation is applied to penalise large gradients in the reconstructed source brightness. The parameters for the lens mass and light profiles are optimised nonlinearly using the MultiNest algorithm (Feroz et al. 2009). The positions of assumed lens images are provided as inputs, with models constrained to ensure that these positions align in the source plane with a tolerance of $1''$. Each model is checked against three criteria: the presence of an SIE critical curve consistent with observed lens image; the alignment of the critical curve with the lens galaxy’s light profile; and finally, the consistency of the reconstructed source with a compact object inside a caustic.

From all the lenses found in the field, we considered the ones that have a convincing model (identified as ‘valid’ in the ‘modelling’ column of table 2 in Acevedo Barroso et al. 2024), and for which the value of the Einstein radius is available. An image of these lenses is shown in Fig. 11. The recovery plot associated to these lenses is shown in Fig. 12. From the figure, we can see that the recovery of the Einstein radius is within 1σ from the ideal equality line for all lenses, except for the lens J031959+414229. Overall, the recovery of the parameter is sufficiently accurate for real *Euclid* lenses. It is remarkable that the lens J031749+420011 is recovered correctly, albeit with a large uncertainty, due to the fact that there is a very bright star present

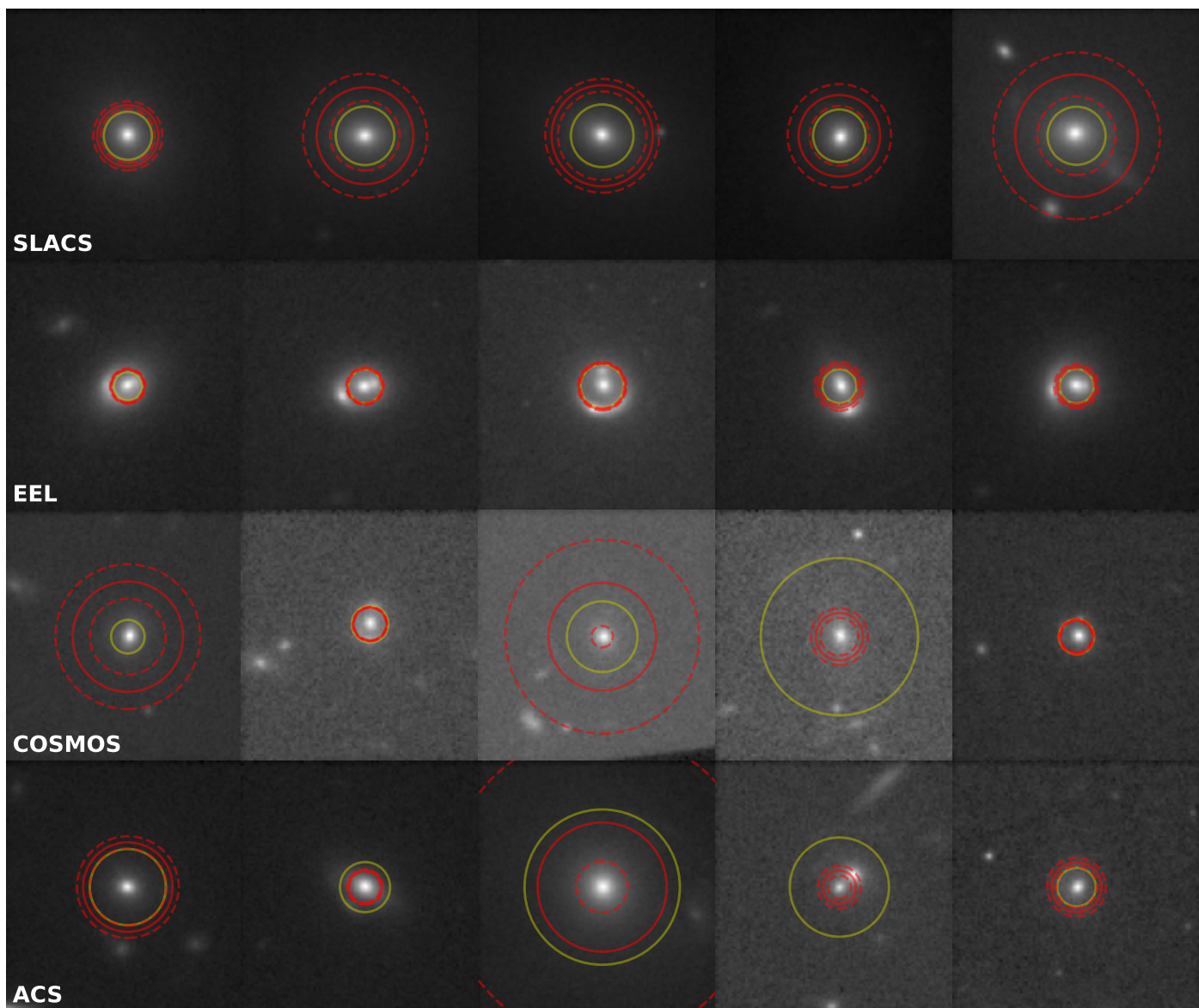


Fig. 9. Random selection of 20 $10'' \times 10''$ cutouts of Euclidised lenses taken from the SLACS, EEL, COSMOS, and ACS subsamples. Red circles show the best predictions for the Einstein radius from LEMON, with corresponding 16th and 84th percentiles shown with dashed red circles. Yellow circles show the values for the Einstein radii reported in Bolton et al. (2008), Oldham et al. (2017), Faure et al. (2008), and Pawase et al. (2014), respectively. For ACS lenses, the radius of the arc is taken instead, due to lack of Einstein radius measurement.

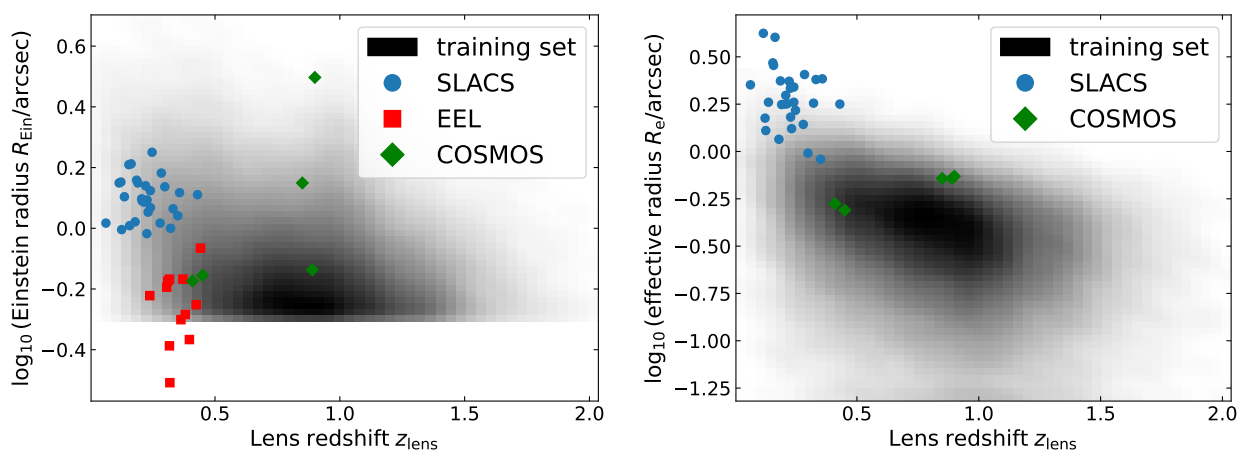


Fig. 10. Distributions of the Einstein radius (left panel) and the lens effective radius (right panel) as a function of lens redshift. Black regions show the training set, while coloured points show the position of the Euclidised lenses.

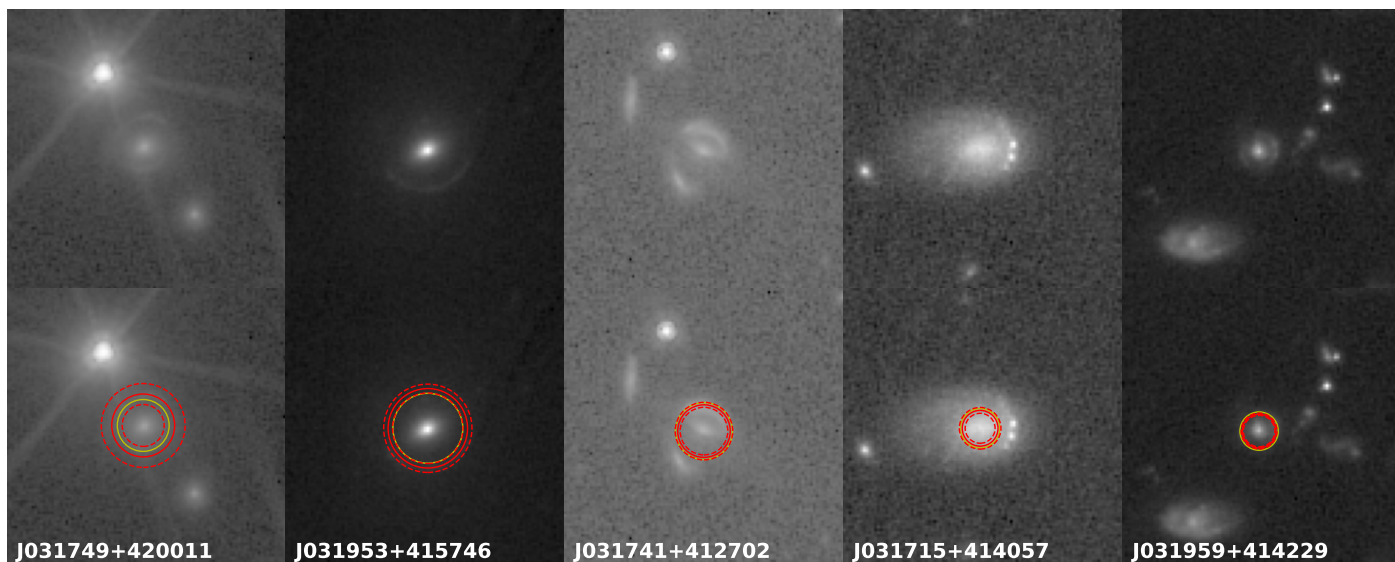


Fig. 11. $10'' \times 10''$ cutouts of the five *Euclid* gravitational lenses found in the Perseus ERO field and modelled in [Acevedo Barroso et al. \(2024\)](#). *Top row*: unedited cutouts centred on the lenses. *Bottom row*: the same cutouts, with the predicted Einstein radius (red circles, with dashed circles showing the uncertainty bands) and the value obtained from the classical modelling (yellow circle) superimposed on them.

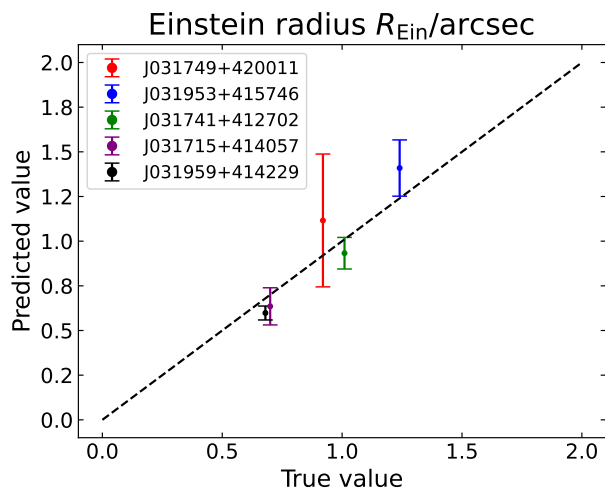


Fig. 12. Same as Fig. 8, but for the *Euclid* lenses found in the Perseus ERO field.

in the cutout, which increases both the aleatoric uncertainty and the epistemic uncertainty, the former due to low visibility of the lens and the latter due to not having trained LEMON with stars as contaminants in the image.

6.3. LEMON applied to real *Euclid* Q1 lenses

We have finally applied LEMON to the sample of strong lens images found by the strong lensing discovery engine in the *Euclid* Quick Release 1 (Q1) data ([Euclid Collaboration: Walmsley et al. 2025](#)). Through an initial scan of the Q1 galaxy catalogues with machine-learning models, followed by citizen science inspection, expert vetting, and system-by-system modelling, [Euclid Collaboration: Walmsley et al. \(2025\)](#) has collected 500 strong lens candidates, divided in Grade A (246) and B (254) lens candidates after the expert vetting scoring. We complement these data with 38 Grade A and 40 Grade B candidates found

Table 4. Same as Table 3, but for the *Euclid* lenses found in the Q1 fields.

Metrics	$R_{\text{Ein}}/\text{arcsec}$
Bias (μ)	0.05
Lower discr. scatter (σ^-)	0.09
Upper discr. scatter (σ^+)	0.22
RMSE	0.36
MAE	0.20
NMAD	0.14
Coefficient of determination (R^2)	0.49

after the expert visual classification performed on high-velocity dispersion galaxies in [Euclid Collaboration: Rojas et al. \(2025\)](#).

The strong lenses in [Euclid Collaboration: Walmsley et al. \(2025\)](#); [Euclid Collaboration: Rojas et al. \(2025\)](#) have been modelled via PyAutoLens, which is the standard algorithm for lens modelling in *Euclid*⁶ ([Nightingale & Dye 2015](#); [Nightingale et al. 2018, 2021b](#)). PyAutoLens is an open-source Python package for strong gravitational lensing, which includes both fully automated strong lens modelling of galaxies and galaxy clusters, and tools for simulating samples of strong lenses. In this work, PyAutoLens employs an SIE mass model, consistent with the model used to train LEMON.

We predicted the Einstein radii of 292 expert-vetted Grade A and B lenses of the first sample and 54 lenses of the second sample, chosen such that the classical modelling of the Einstein radius is successful, achieving a good agreement with the predictions obtained via PyAutoLens, as shown in Fig. 13. The metrics, presented in Table 4, indicate a sufficiently good recovery, with an R^2 value of 0.49. The bias and NMAD are both very low, respectively $0''.05$ and $0''.14$, showing only a slight skew towards higher values with respect to the predictions of PyAutoLens, indicated by the value of $\sigma^+ = 0''.22$. Overall, these results show that LEMON is a robust estimator of the Einstein radius for real *Euclid* lenses.

⁶ <https://github.com/Jammy2211/PyAutoLens>

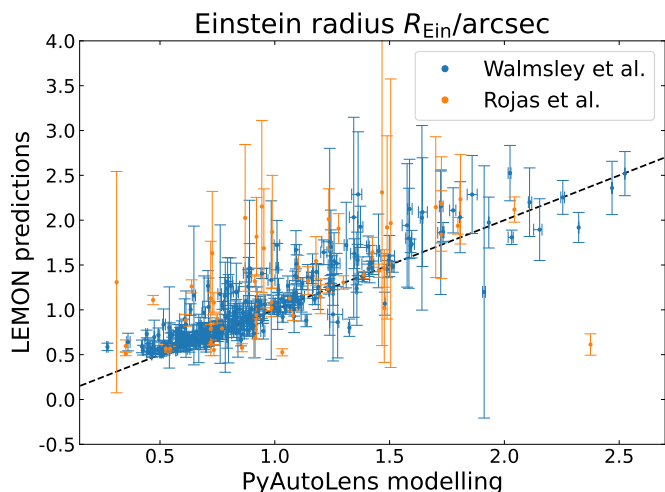


Fig. 13. Same as Figs. 8 and 12, but for the *Euclid* lenses found in the Q1 fields.

7. Speed-up of traditional methods due to LEMON

One possible use of LEMON in the context of strong lensing applications within *Euclid*, beside fast modelling of strong gravitational lenses, is to speed-up the modelling of strong gravitational lenses by giving traditional lens modelling methods initial starting points from which to start the search.

To perform lens modelling, PyAutoLens adopts the Python library PyAutoFit⁷ (Nightingale et al. 2021a). The standard modelling pipeline uses nested-sampling algorithms, such as *nautilus* (Lange 2023), for Bayesian inference of the lens model. To efficiently use the information from LEMON, PyAutoLens can use a gradient ascent optimiser, which fully exploits the information from the initial starting point (Amorisco et al. 2022). The lens light and source galaxy during lens modelling are modelled using a Multi-Gaussian expansion (MGE) technique (see He et al. 2024), independent of any information provided by LEMON, most notably meaning that, when using the gradient ascent optimiser, the centre of the source galaxy uses an initial starting point at $(0'', 0'')$.

To assess the speed gain in doing so, we considered 20 random lenses from the test sample of *Euclid* mock lenses, and first modelled them through PyAutoLens with the standard modelling pipeline. The modelling took approximately 25 000 likelihood evaluations, which amount to around 7 h on a single CPU. A total of 19 out of 20 fits successfully recover the input Einstein radius and other parameters, demonstrating the reliability of the PyAutoLens standard modelling pipeline. However, in one case, the fit is biased due to additional line-of-sight emission from a galaxy not associated with the strong lens (a future iteration of the PyAutoLens pipeline will include modelling emission from line-of-sight galaxies).

We use PyAutoLens with the gradient ascent optimiser, by modelling the lenses with LEMON and then using the obtained best values as starting point for the optimiser. The fits take about 1000 likelihood evaluations, which amounts to around 0.27 h on a single CPU, which is a substantial gain over the standard modelling pipeline. The majority of the fits are good, except for three of the lenses, which return a wrong lens model with respect to the standard modelling. The cause of this is the fact that LEMON does not provide a source centre, so the starting point for it is

$(0'', 0'')$. This implies that the maximum likelihood estimator could shoot off in the wrong direction due to the wrong starting point for the source centre, and give a wrong model estimation. If an estimate of the source centre is available, the faster combination of LEMON initial starting point plus gradient ascent algorithm works in all cases, and is 26 times faster than the standard modelling pipeline on simulations. This speed-up of modelling is consistent with results from Pearson et al. (2021), where a BNN was used to predict gravitational lens parameters, which are then given to PyAutoLens as priors. In their case, the combination of BNN and PyAutoLens increased the modelling speed by a mean factor of 1.73. It should be noted, however, that in our case the standard modelling method is not a Markov chain Monte Carlo with priors set by a BNN like in Pearson et al. (2021), and as such, the speed-up factor in our case can be bigger due to the use of a simpler algorithm. This is an optimistic estimate of the speed-up however, given that on real images the predictions from LEMON will be worse than on simulated lenses. In future iterations of LEMON, we aim to also predict the source centre, so that this new approach can be fully implemented. We also plan to implement error estimation on the lens model parameters predicted by PyAutoLens, which are currently not computed with the gradient-ascent method. This can be achieved in different ways, for example by using Hessian matrix estimation or the Fisher information matrix. Investigating these approaches is, however, beyond the scope of this paper.

Finally, to assess whether the optimiser approach needs LEMON in order to correctly model gravitational lenses, we repeated the test by using random starting points for the optimiser. Results show that, with random initialisations, PyAutoLens is unable to successfully recover a correct lens model fit for any of the lenses. Thus, the robust initial starting points provided by LEMON prove to be required in order for PyAutoLens to be sped up by using the gradient ascent optimiser instead of the nested sampling algorithm.

An important benefit of combining LEMON and PyAutoLens lies in their ability to complement each other's limitations. For instance, the standard PyAutoLens modelling pipeline inferred an incorrect lens model for one system due to misinterpreting additional line-of-sight emission from an unrelated interloper galaxy as part of the lensed source. By using LEMON as a starting point, the initial solution was already aligned with the strong lens, allowing PyAutoLens to refine the model through gradient ascent without being misled by interloper emission. Running independent fits with both the standard PyAutoLens pipeline and the combined LEMON-PyAutoLens approach for the same lens, and selecting the best-fit model from the two therefore provides a viable strategy to minimise failure rates in lens modelling.

8. Conclusions

In this work, we expand the lens modelling machine-learning algorithm LEMON (Gentile et al. 2023) by predicting both the mass and the light of the foreground deflector of *Euclid* galaxy-galaxy gravitational lenses. The former is modelled as an SIE without external shear, while the latter is a single Sérsic profile. We used mock *Euclid* lenses with contaminants in the image for both training and testing of the architecture. The main results are as follows.

- All parameters of the test set are recovered correctly, with very low values of bias and scatter. The parameter that is recovered worst is the Sérsic index, which shows a large scatter

⁷ <https://github.com/rhayes777/PyAutoFit>

and a deviation from the linear trend for high values of the Sérsic index. This suggests that LEMON is able to recover the mass and light parameters for the lens even in the presence of companions contaminating the image.

- The epistemic uncertainties are systematically lower than the aleatoric uncertainties, which is consistent with a training set that correctly spanned the parameter space.
- Applied to a selection of Euclidised HST images, LEMON manages to recover Einstein radius, axis ratio, position angle, and lens effective radius of the lens, while we cannot reach any conclusion on the Sérsic index due to low statistics. As expected, in general results are worse than those obtained from the test set, given that Euclidised lenses have a much worse S/N than the simulated lenses, and may not be similar to the simulations used to train the network, as shown in Fig. 10. It should also be noted that both SLACS and ACS lenses have been modelled by assuming a De Vaucouleurs light profile, while LEMON assumes a Sérsic profile with variable values for the Sérsic index, and as such the associated true values for the lens effective radius cannot be compared homogeneously with the LEMON predictions. Moreover, a number of lenses have effective radii bigger than $2''$, which is the upper limit of the respective training sample for LEMON, and as such their predictions are unreliable extrapolations, and have not been reported. In the future, we will expand the training sample to include lenses with effective radii bigger than $2''$.
- Applied to five real galaxy-galaxy *Euclid* gravitational lenses observed in the Perseus ERO field and the 578 new candidates in the Q1 data (Acevedo Barroso et al. 2024; Euclid Collaboration: Walmsley et al. 2025; Euclid Collaboration: Rojas et al. 2025), for which the value of the Einstein radius is available thanks to classical modelling, we obtain an accurate recovery of the parameter for all lenses.
- By using the predictions of LEMON as starting points for PyAutoLens, it is possible to speed up the algorithm by up to 26 times compared to the standard *Euclid* modelling pipeline. This would not be possible without the initial LEMON guesses, because the gradient-ascent optimiser with random initialisations does not produce valid model results for all lenses.

In future works, we plan to further advance the LEMON architecture, by predicting the parameters of more general lens mass models, such as the power-law model. We also plan on enhancing the prediction of certain parameters by deblending the gravitational lens image in lens-only and source-only images (Zhong et al. 2024), and train LEMON separately on the two components. We will also test in more detail the recovery of the lens light parameters, predicting values of effective radius and Sérsic index of real *Euclid* data, when they will become available. Finally, we will try to upgrade LEMON to also predict the parameters of the source, especially its position, given its usefulness in enhancing the performance of the *Euclid* standard modelling pipeline.

Q1 data are now public, with DR1 data around the corner. We are therefore preparing to process the enormous amount of upcoming data, and have started applying LEMON to newly discovered strong lenses from the Q1 data release. Results confirm that LEMON is a robust and fast lens modelling tool for *Euclid*. This will enable the generation of models for the approximately 100 000 expected *Euclid* lenses in a remarkably short time.

By applying LEMON and PyAutoLens to *Euclid* gravitational lenses, we will determine the total mass within the Einstein radius, or extrapolated to the effective radius, when lens and

source redshifts are available. Combining this with stellar mass estimates from SED fitting (Euclid Collaboration: Enia et al. 2025), we will derive dark matter fractions. We will also provide constraints on the mass density slope and initial mass function. With such a vast statistical lens sample, we will be able to investigate the evolution of these properties in unprecedented detail, as well as the scaling relations which relate them as a function of redshift (Koopmans et al. 2006; Gavazzi et al. 2007; Bolton et al. 2008; Auger et al. 2010; Tortora et al. 2010, 2014, 2018, 2019; Sonnenfeld et al. 2013, 2015, 2017; O’Riordan et al. 2025). By comparing these scaling relations with predictions from cosmological simulations, we will be able to constrain cosmological parameters and physical processes in galaxies (Mukherjee et al. 2018, 2021, 2022; Busillo et al. 2023, 2025; Tortora et al. 2025).

Acknowledgements. VB and CT acknowledge the INAF grant 2022 LEMON. LL thanks the support from INAF theory Grant 2022: Illuminating Dark Matter using Weak Lensing by Cluster Satellites. This research uses observations made with the NASA/ESA Hubble Space Telescope obtained from the Space Telescope Science Institute, which is operated by the Association of Universities for Research in Astronomy, Inc., under NASA contract NAS 5–26555. This work has made use of the Early Release Observations (ERO) data from the *Euclid* mission of the European Space Agency (ESA), 2024, <https://doi.org/10.57780/esa-qmocz3>. This work has made use of the *Euclid* Quick Release Q1 data from the *Euclid* mission of the European Space Agency (ESA), 2025, <https://doi.org/10.57780/esa-2853f3b>. The Euclid Consortium acknowledges the European Space Agency and a number of agencies and institutes that have supported the development of *Euclid*, in particular the Agenzia Spaziale Italiana, the Austrian Forschungsförderungsgesellschaft funded through BMK, the Belgian Science Policy, the Canadian Euclid Consortium, the Deutsches Zentrum für Luft- und Raumfahrt, the DTU Space and the Niels Bohr Institute in Denmark, the French Centre National d’Etudes Spatiales, the Fundação para a Ciência e a Tecnologia, the Hungarian Academy of Sciences, the Ministerio de Ciencia, Innovación y Universidades, the National Aeronautics and Space Administration, the National Astronomical Observatory of Japan, the Nederlandse Onderzoekschool Voor Astronomie, the Norwegian Space Agency, the Research Council of Finland, the Romanian Space Agency, the State Secretariat for Education, Research, and Innovation (SERI) at the Swiss Space Office (SSO), and the United Kingdom Space Agency. A complete and detailed list is available on the *Euclid* web site (www.euclid-ec.org).

References

- Abadi, M., Agarwal, A., Barham, P., et al. 2015, TensorFlow: Large-Scale Machine Learning on Heterogeneous Systems, software available from tensorflow.org
- Acevedo Barroso, J. A., O’Riordan, C. M., Clément, B., et al. 2024, A&A, submitted, arXiv:2408.06217
- Amorisco, N. C., Nightingale, J., He, Q., et al. 2022, MNRAS, 510, 2464
- Atek, H., Gavazzi, R., Weaver, J. R., et al. 2024, arXiv:2405.13504
- Auger, M. W., Treu, T., Bolton, A. S., et al. 2009, ApJ, 705, 1099
- Auger, M. W., Treu, T., Bolton, A. S., et al. 2010, ApJ, 724, 511
- Bolton, A. S., Burles, S., Koopmans, L. V. E., et al. 2008, ApJ, 682, 964
- Bradley, L., Sipőcz, B., Robitaille, T., et al. 2023, astropy/photutils: 1.8.0
- Busillo, V., Tortora, C., Covone, G., et al. 2025, A&A, 693, A112
- Busillo, V., Tortora, C., Napolitano, N. R., et al. 2023, MNRAS, 525, 6191
- Cañameras, R., Schuldt, S., Suyu, S., et al. 2020, A&A, 644, A163
- Charnock, T., Perreault-Levasseur, L., & Lanusse, F. 2020, arXiv:2006.01490
- Coe, D., Zitrin, A., Carrasco, M., et al. 2013, ApJ, 762, 32
- Cuillandre, J. C., Bertin, E., Bolzonella, M., et al. 2024a, arXiv:2405.13496
- Cuillandre, J. C., Bolzonella, M., Boselli, A., et al. 2024b, arXiv:2405.13501
- Euclid Collaboration: Aussel, H., Tereno, I., Schirmer, M., et al. 2025, A&A, submitted
- Euclid Collaboration: Castander, F., Fosalba, P., Stadel, J., et al. 2024, A&A, accepted, arXiv:2405.13495
- Euclid Collaboration: Cropper, M., Al-Bahlawan, A., Amiaux, J., et al. 2024, arXiv:2405.13492
- Euclid Collaboration: Enia, A., Pozzetti, L., Bolzonella, M., et al. 2025, A&A, submitted
- Euclid Collaboration: Holloway, P., Verma, A., Walmsley, M., et al. 2025, A&A, submitted
- Euclid Collaboration: Li, T., Collett, T., Walmsley, M., et al. 2025, A&A, submitted

- Euclid Collaboration: Lines, N. E. P., Collett, T. E., Walmsley, M., et al. 2025, *A&A*, submitted
- Euclid Collaboration: Mellier, Y., Abdurro'uf, Acevedo Barroso, J. A., et al. 2024, arXiv:2405.13491
- Euclid Collaboration: Rojas, K., Collett, T., Acevedo Barroso, J., et al. 2025, *A&A*, submitted
- Euclid Collaboration: Scaramella, R., Amiaux, J., Mellier, Y., et al. 2022, *A&A*, 662, A112
- Euclid Collaboration: Walmsley, M., Holloway, P., Lines, N., et al. 2025, *A&A*, submitted
- Euclid Early Release Observations. 2024, <https://doi.org/10.57780/esa-qmocz3>
- Euclid Quick Release Q1. 2025, <https://doi.org/10.57780/esa-2853f3b>
- Faure, C., Kneib, J.-P., Covone, G., et al. 2008, *ApJS*, 176, 19
- Feroz, F., Hobson, M. P., & Bridges, M. 2009, *MNRAS*, 398, 1601
- Gavazzi, R., Treu, T., Marshall, P. J., Braut, F., & Ruff, A. 2012, *ApJ*, 761, 170
- Gavazzi, R., Treu, T., Rhodes, J. D., et al. 2007, *ApJ*, 667, 176
- Gentile, F., Tortora, C., Covone, G., et al. 2023, *MNRAS*, 522, 5442
- Guo, C., Pleiss, G., Sun, Y., & Weinberger, K. Q. 2017, in *Proceedings of Machine Learning Research*, Vol. 70, *Proceedings of the 34th International Conference on Machine Learning*, ed. D. Precup & Y. W. Teh (PMLR), 1321–1330
- Harvey-Hawes, C. & Wiltshire, D. L. 2024, *MNRAS*, 534, 3364
- He, K., Zhang, X., Ren, S., & Sun, J. 2015, arXiv:1512.03385
- He, Q., Nightingale, J. W., Amvrosiadis, A., et al. 2024, *MNRAS*, 532, 2441
- Hunt, L., Annibali, F., Cuillandre, J.-C., et al. 2024, *A&A*, accepted, arXiv:2405.13499
- Keeton, C. 2016, *Methods for strong lens modelling*, ed. E. Mediavilla, J. A. Muñoz, F. Garzón, & T. J. Mahoney, *Canary Islands Winter School of Astrophysics* (Cambridge University Press), 213–250
- Kingma, D. P. & Ba, J. 2015, in *3rd International Conference on Learning Representations, ICLR 2015, San Diego, CA, USA, May 7-9, 2015, Conference Track Proceedings*, ed. Y. Bengio & Y. LeCun
- Kluge, M., Hatch, N. A., Montes, M., et al. 2024, arXiv:2405.13503
- Koopmans, L. V. E., Bolton, A., Treu, T., et al. 2009, *ApJ*, 703, L51
- Koopmans, L. V. E., Treu, T., Bolton, A. S., Burles, S., & Moustakas, L. A. 2006, *ApJ*, 649, 599
- Kull, M., Filho, T. S., & Flach, P. 2017, in *Proceedings of Machine Learning Research*, Vol. 54, *Proceedings of the 20th International Conference on Artificial Intelligence and Statistics*, ed. A. Singh & J. Zhu (PMLR), 623–631
- Lange, J. U. 2023, *MNRAS*, 525, 3181
- Laureijs, R., Amiaux, J., Arduini, S., et al. 2011, *ESA/SRE(2011)12*, arXiv:1110.3193
- Li, R., Napolitano, N. R., Roy, N., et al. 2022, *ApJ*, 929, 152
- Li, R., Napolitano, N. R., Tortora, C., et al. 2020, *ApJ*, 899, 30
- Marleau, F. R., Cuillandre, J. C., Cantiello, M., et al. 2024, arXiv:2405.13502
- Massari, D., Dalessandro, E., Erkal, D., et al. 2024, arXiv:2405.13498
- Meneghetti, M., Cui, W., Rasia, E., et al. 2023, *A&A*, 678, L2
- Meneghetti, M., Davoli, G., Bergamini, P., et al. 2020, *Science*, 369, 1347
- Meneghetti, M., Melchior, P., Grazian, A., et al. 2008, *A&A*, 482, 403
- Meneghetti, M., Ragagnin, A., Borgani, S., et al. 2022, *A&A*, 668, A188
- Meneghetti, M., Rasia, E., Merten, J., et al. 2010, *A&A*, 514, A93
- Metcalfe, R. B., Meneghetti, M., Avetruz, C., et al. 2019, *A&A*, 625, A119
- Mukherjee, S., Koopmans, L. V. E., Metcalfe, R. B., et al. 2018, *MNRAS*, 479, 4108
- Mukherjee, S., Koopmans, L. V. E., Metcalfe, R. B., et al. 2021, *MNRAS*, 504, 3455
- Mukherjee, S., Koopmans, L. V. E., Tortora, C., et al. 2022, *MNRAS*, 509, 1245
- Nagam, B. C., Acevedo Barroso, J. A., Wilde, J., et al. 2025, *A&A*, submitted, arXiv:2502.09802
- Nagam, B. C., Koopmans, L. V. E., Valentijn, E. A., et al. 2024, *MNRAS*, 533, 1426
- Nightingale, J. W. & Dye, S. 2015, *MNRAS*, 452, 2940
- Nightingale, J. W., Dye, S., & Massey, R. J. 2018, *MNRAS*, 478, 4738
- Nightingale, J. W., Hayes, R. G., & Griffiths, M. 2021a, *Journal of Open Source Software*, 6, 2550
- Nightingale, J. W., Hayes, R. G., Kelly, A., et al. 2021b, *Journal of Open Source Software*, 6, 2825
- Oldham, L., Auger, M. W., Fassnacht, C. D., et al. 2017, *MNRAS*, 465, 3185
- O'Riordan, C. M., Oldham, L. J., Nersesian, A., et al. 2025, *A&A*, 694, A145
- Pawase, R. S., Courbin, F., Faure, C., Kokotanekova, R., & Meylan, G. 2014, *MNRAS*, 439, 3392
- Pearce-Casey, R., Nagam, B. C., Wilde, J., et al. 2024, *A&A*, submitted, arXiv:2411.16808
- Pearson, J., Li, N., & Dye, S. 2019, *MNRAS*, 488, 991
- Pearson, J., Maresca, J., Li, N., & Dye, S. 2021, *MNRAS*, 505, 4362
- Perreault Levasseur, L., Hezaveh, Y. D., & Wechsler, R. H. 2017, *ApJ*, 850, L7
- Petrillo, C. E., Tortora, C., Chatterjee, S., et al. 2019a, *MNRAS*, 482, 807
- Petrillo, C. E., Tortora, C., Chatterjee, S., et al. 2017, *MNRAS*, 472, 1129
- Petrillo, C. E., Tortora, C., Vernardos, G., et al. 2019b, *MNRAS*, 484, 3879
- Powell, D., Vegetti, S., McKean, J. P., et al. 2021, *MNRAS*, 501, 515
- Rezaei, S., McKean, J. P., Biehl, M., de Roo, W., & Lafontaine, A. 2022, *MNRAS*, 517, 1156
- Ritondale, E., Vegetti, S., Despali, G., et al. 2019, *MNRAS*, 485, 2179
- Rizzo, F., Vegetti, S., Fraternali, F., & Di Teodoro, E. 2018, *MNRAS*, 481, 5606
- Rojas, K., Savary, E., Clément, B., et al. 2022, *A&A*, 668, A73
- Russakovsky, O., Deng, J., Su, H., et al. 2015, *International Journal of Computer Vision (IJCV)*, 115, 211
- Rybak, M., McKean, J. P., Vegetti, S., Andreani, P., & White, S. D. M. 2015a, *MNRAS*, 451, L40
- Rybak, M., Vegetti, S., McKean, J. P., Andreani, P., & White, S. D. M. 2015b, *MNRAS*, 453, L26
- Saifollahi, T., Voggel, K., Lançon, A., et al. 2024, arXiv:2405.13500
- Schuldt, S., Suyu, S. H., Cañameras, R., et al. 2023, *A&A*, 673, A33
- Schuldt, S., Suyu, S. H., Meinhardt, T., et al. 2021, *A&A*, 646, A126
- Scoville, N., Aussel, H., Benson, A., et al. 2007, *ApJS*, 172, 150
- Sengül, A. Ç. & Dvorkin, C. 2022, *MNRAS*, 516, 336
- Shajib, A. J., Treu, T., Birrer, S., & Sonnenfeld, A. 2021, *MNRAS*, 503, 2380
- Sonnenfeld, A., Nipoti, C., & Treu, T. 2017, *MNRAS*, 465, 2397
- Sonnenfeld, A., Treu, T., Gavazzi, R., et al. 2013, *ApJ*, 777, 98
- Sonnenfeld, A., Treu, T., Marshall, P. J., et al. 2015, *ApJ*, 800, 94
- Tortora, C., Busillo, V., Napolitano, N. R., et al. 2025, arXiv:2502.13589
- Tortora, C., La Barbera, F., Napolitano, N. R., et al. 2014, *MNRAS*, 445, 115
- Tortora, C., Napolitano, N. R., Romanowsky, A. J., & Jetzer, P. 2010, *ApJ*, 721, L1
- Tortora, C., Napolitano, N. R., Roy, N., et al. 2018, *MNRAS*, 473, 969
- Tortora, C., Posti, L., Koopmans, L. V. E., & Napolitano, N. R. 2019, *MNRAS*, 489, 5483
- Treu, T., Auger, M. W., Koopmans, L. V. E., et al. 2010, *ApJ*, 709, 1195
- Vegetti, S. & Koopmans, L. V. E. 2009, *MNRAS*, 392, 945
- Vegetti, S., Koopmans, L. V. E., Bolton, A., Treu, T., & Gavazzi, R. 2010, *MNRAS*, 408, 1969
- Weaver, J. R., Kauffmann, O. B., Ilbert, O., et al. 2022, *ApJS*, 258, 11
- Zhong, F., Luo, R., Napolitano, N. R., et al. 2024, arXiv:2410.02936

¹ INAF-Osservatorio Astronomico di Capodimonte, Via Moiriello 16, 80131 Napoli, Italy

² Department of Physics "E. Pancini", University Federico II, Via Cinthia 6, 80126, Napoli, Italy

³ INFN section of Naples, Via Cinthia 6, 80126, Napoli, Italy

⁴ Dipartimento di Fisica e Astronomia "Augusto Righi" - Alma Mater Studiorum Università di Bologna, via Piero Gobetti 93/2, 40129 Bologna, Italy

⁵ INAF-Osservatorio di Astrofisica e Scienza dello Spazio di Bologna, Via Piero Gobetti 93/3, 40129 Bologna, Italy

⁶ School of Mathematics, Statistics and Physics, Newcastle University, Herschel Building, Newcastle-upon-Tyne, NE1 7RU, UK

⁷ INFN-Sezione di Bologna, Viale Berti Pichat 6/2, 40127 Bologna, Italy

⁸ CEA Saclay, DFR/IRFU, Service d'Astrophysique, Bat. 709, 91191 Gif-sur-Yvette, France

⁹ Dipartimento di Fisica e Astronomia, Università di Bologna, Via Gobetti 93/2, 40129 Bologna, Italy

¹⁰ Aix-Marseille Université, CNRS, CNES, LAM, Marseille, France

¹¹ Institut d'Astrophysique de Paris, UMR 7095, CNRS, and Sorbonne Université, 98 bis boulevard Arago, 75014 Paris, France

¹² School of Physics and Astronomy, Sun Yat-sen University, Guangzhou 519082, Zhuhai Campus, China

¹³ Institute for Astrophysics, School of Physics, Zhengzhou University, Zhengzhou, 450001, China

¹⁴ Institute of Physics, Laboratory of Astrophysics, Ecole Polytechnique Fédérale de Lausanne (EPFL), Observatoire de Sauverny, 1290 Versoix, Switzerland

¹⁵ SCITAS, Ecole Polytechnique Fédérale de Lausanne (EPFL), 1015 Lausanne, Switzerland

¹⁶ Dipartimento di Fisica "E. Pancini", Università degli Studi di Napoli Federico II, Via Cinthia 6, 80126, Napoli, Italy

¹⁷ Institut de Ciències del Cosmos (ICCUB), Universitat de Barcelona (IEEC-UB), Martí i Franquès 1, 08028 Barcelona, Spain

¹⁸ Institució Catalana de Recerca i Estudis Avançats (ICREA), Passeig de Lluís Companys 23, 08010 Barcelona, Spain

¹⁹ David A. Dunlap Department of Astronomy & Astrophysics, University of Toronto, 50 St George Street, Toronto, Ontario M5S 3H4, Canada

- ²⁰ Jodrell Bank Centre for Astrophysics, Department of Physics and Astronomy, University of Manchester, Oxford Road, Manchester M13 9PL, UK
- ²¹ School of Physical Sciences, The Open University, Milton Keynes, MK7 6AA, UK
- ²² Department of Physics and Astronomy, University of British Columbia, Vancouver, BC V6T 1Z1, Canada
- ²³ Laboratoire d'étude de l'Univers et des phénomènes eXtremes, Observatoire de Paris, Université PSL, Sorbonne Université, CNRS, 92190 Meudon, France
- ²⁴ Université Paris-Saclay, CNRS, Institut d'astrophysique spatiale, 91405, Orsay, France
- ²⁵ ESAC/ESA, Camino Bajo del Castillo, s/n., Urb. Villafranca del Castillo, 28692 Villanueva de la Cañada, Madrid, Spain
- ²⁶ School of Mathematics and Physics, University of Surrey, Guildford, Surrey, GU2 7XH, UK
- ²⁷ INAF-Osservatorio Astronomico di Brera, Via Brera 28, 20122 Milano, Italy
- ²⁸ Université Paris-Saclay, Université Paris Cité, CEA, CNRS, AIM, 91191, Gif-sur-Yvette, France
- ²⁹ IFPU, Institute for Fundamental Physics of the Universe, via Beirut 2, 34151 Trieste, Italy
- ³⁰ INAF-Osservatorio Astronomico di Trieste, Via G. B. Tiepolo 11, 34143 Trieste, Italy
- ³¹ INFN, Sezione di Trieste, Via Valerio 2, 34127 Trieste TS, Italy
- ³² SISSA, International School for Advanced Studies, Via Bonomea 265, 34136 Trieste TS, Italy
- ³³ Dipartimento di Fisica, Università di Genova, Via Dodecaneso 33, 16146, Genova, Italy
- ³⁴ INFN-Sezione di Genova, Via Dodecaneso 33, 16146, Genova, Italy
- ³⁵ Instituto de Astrofísica e Ciências do Espaço, Universidade do Porto, CAUP, Rua das Estrelas, PT4150-762 Porto, Portugal
- ³⁶ Faculdade de Ciências da Universidade do Porto, Rua do Campo de Alegre, 4150-007 Porto, Portugal
- ³⁷ Dipartimento di Fisica, Università degli Studi di Torino, Via P. Giuria 1, 10125 Torino, Italy
- ³⁸ INFN-Sezione di Torino, Via P. Giuria 1, 10125 Torino, Italy
- ³⁹ INAF-Osservatorio Astrofisico di Torino, Via Osservatorio 20, 10025 Pino Torinese (TO), Italy
- ⁴⁰ European Space Agency/ESTEC, Keplerlaan 1, 2201 AZ Noordwijk, The Netherlands
- ⁴¹ Institute Lorentz, Leiden University, Niels Bohrweg 2, 2333 CA Leiden, The Netherlands
- ⁴² Leiden Observatory, Leiden University, Einsteinweg 55, 2333 CC Leiden, The Netherlands
- ⁴³ INAF-IASF Milano, Via Alfonso Corti 12, 20133 Milano, Italy
- ⁴⁴ INAF-Osservatorio Astronomico di Roma, Via Frascati 33, 00078 Monteporzio Catone, Italy
- ⁴⁵ INFN-Sezione di Roma, Piazzale Aldo Moro, 2 - c/o Dipartimento di Fisica, Edificio G. Marconi, 00185 Roma, Italy
- ⁴⁶ Centro de Investigaciones Energéticas, Medioambientales y Tecnológicas (CIEMAT), Avenida Complutense 40, 28040 Madrid, Spain
- ⁴⁷ Port d'Informació Científica, Campus UAB, C. Albareda s/n, 08193 Bellaterra (Barcelona), Spain
- ⁴⁸ Institute for Theoretical Particle Physics and Cosmology (TTK), RWTH Aachen University, 52056 Aachen, Germany
- ⁴⁹ Institute for Astronomy, University of Hawaii, 2680 Woodlawn Drive, Honolulu, HI 96822, USA
- ⁵⁰ Dipartimento di Fisica e Astronomia "Augusto Righi" - Alma Mater Studiorum Università di Bologna, Viale Berti Pichat 6/2, 40127 Bologna, Italy
- ⁵¹ Instituto de Astrofísica de Canarias, Vía Láctea, 38205 La Laguna, Tenerife, Spain
- ⁵² Institute for Astronomy, University of Edinburgh, Royal Observatory, Blackford Hill, Edinburgh EH9 3HJ, UK
- ⁵³ European Space Agency/ESRIN, Largo Galileo Galilei 1, 00044 Frascati, Roma, Italy
- ⁵⁴ Université Claude Bernard Lyon 1, CNRS/IN2P3, IP2I Lyon, UMR 5822, Villeurbanne, F-69100, France
- ⁵⁵ UCB Lyon 1, CNRS/IN2P3, IUF, IP2I Lyon, 4 rue Enrico Fermi, 69622 Villeurbanne, France
- ⁵⁶ Mullard Space Science Laboratory, University College London, Holmbury St Mary, Dorking, Surrey RH5 6NT, UK
- ⁵⁷ Departamento de Física, Faculdade de Ciências, Universidade de Lisboa, Edifício C8, Campo Grande, PT1749-016 Lisboa, Portugal
- ⁵⁸ Instituto de Astrofísica e Ciências do Espaço, Faculdade de Ciências, Universidade de Lisboa, Campo Grande, 1749-016 Lisboa, Portugal
- ⁵⁹ Department of Astronomy, University of Geneva, ch. d'Ecogia 16, 1290 Versoix, Switzerland
- ⁶⁰ INAF-Istituto di Astrofisica e Planetologia Spaziali, via del Fosso del Cavaliere, 100, 00100 Roma, Italy
- ⁶¹ INFN-Padova, Via Marzolo 8, 35131 Padova, Italy
- ⁶² Aix-Marseille Université, CNRS/IN2P3, CPPM, Marseille, France
- ⁶³ Space Science Data Center, Italian Space Agency, via del Politecnico snc, 00133 Roma, Italy
- ⁶⁴ INFN-Bologna, Via Irnerio 46, 40126 Bologna, Italy
- ⁶⁵ School of Physics, HH Wills Physics Laboratory, University of Bristol, Tyndall Avenue, Bristol, BS8 1TL, UK
- ⁶⁶ Universitäts-Sternwarte München, Fakultät für Physik, Ludwig-Maximilians-Universität München, Scheinerstrasse 1, 81679 München, Germany
- ⁶⁷ Max Planck Institute for Extraterrestrial Physics, Giessenbachstr. 1, 85748 Garching, Germany
- ⁶⁸ INAF-Osservatorio Astronomico di Padova, Via dell'Osservatorio 5, 35122 Padova, Italy
- ⁶⁹ Institute of Theoretical Astrophysics, University of Oslo, P.O. Box 1029 Blindern, 0315 Oslo, Norway
- ⁷⁰ Jet Propulsion Laboratory, California Institute of Technology, 4800 Oak Grove Drive, Pasadena, CA, 91109, USA
- ⁷¹ Department of Physics, Lancaster University, Lancaster, LA1 4YB, UK
- ⁷² Felix Hormuth Engineering, Goethestr. 17, 69181 Leimen, Germany
- ⁷³ Technical University of Denmark, Elektrovej 327, 2800 Kgs. Lyngby, Denmark
- ⁷⁴ Cosmic Dawn Center (DAWN), Denmark
- ⁷⁵ Max-Planck-Institut für Astronomie, Königstuhl 17, 69117 Heidelberg, Germany
- ⁷⁶ NASA Goddard Space Flight Center, Greenbelt, MD 20771, USA
- ⁷⁷ Department of Physics and Astronomy, University College London, Gower Street, London WC1E 6BT, UK
- ⁷⁸ Department of Physics and Helsinki Institute of Physics, Gustaf Hällströmin katu 2, 00014 University of Helsinki, Finland
- ⁷⁹ Université de Genève, Département de Physique Théorique and Centre for Astroparticle Physics, 24 quai Ernest-Ansermet, CH-1211 Genève 4, Switzerland
- ⁸⁰ Department of Physics, P.O. Box 64, 00014 University of Helsinki, Finland
- ⁸¹ Helsinki Institute of Physics, Gustaf Hällströmin katu 2, University of Helsinki, Helsinki, Finland
- ⁸² Centre de Calcul de l'IN2P3/CNRS, 21 avenue Pierre de Coubertin 69627 Villeurbanne Cedex, France
- ⁸³ SKA Observatory, Jodrell Bank, Lower Withington, Macclesfield, Cheshire SK11 9FT, UK
- ⁸⁴ Dipartimento di Fisica "Aldo Pontremoli", Università degli Studi di Milano, Via Celoria 16, 20133 Milano, Italy
- ⁸⁵ INFN-Sezione di Milano, Via Celoria 16, 20133 Milano, Italy
- ⁸⁶ Universität Bonn, Argelander-Institut für Astronomie, Auf dem Hügel 71, 53121 Bonn, Germany
- ⁸⁷ Department of Physics, Institute for Computational Cosmology, Durham University, South Road, Durham, DH1 3LE, UK
- ⁸⁸ Université Côte d'Azur, Observatoire de la Côte d'Azur, CNRS, Laboratoire Lagrange, Bd de l'Observatoire, CS 34229, 06304 Nice cedex 4, France
- ⁸⁹ Université Paris Cité, CNRS, Astroparticule et Cosmologie, 75013 Paris, France

- ⁹⁰ CNRS-UCB International Research Laboratory, Centre Pierre Binetruy, IRL2007, CPB-IN2P3, Berkeley, USA
- ⁹¹ Institut d'Astrophysique de Paris, 98bis Boulevard Arago, 75014, Paris, France
- ⁹² Aurora Technology for European Space Agency (ESA), Camino bajo del Castillo, s/n, Urbanizacion Villafranca del Castillo, Villanueva de la Cañada, 28692 Madrid, Spain
- ⁹³ Institut de Física d'Altes Energies (IFAE), The Barcelona Institute of Science and Technology, Campus UAB, 08193 Bellaterra (Barcelona), Spain
- ⁹⁴ DARK, Niels Bohr Institute, University of Copenhagen, Jagtvej 155, 2200 Copenhagen, Denmark
- ⁹⁵ Centre National d'Etudes Spatiales – Centre spatial de Toulouse, 18 avenue Edouard Belin, 31401 Toulouse Cedex 9, France
- ⁹⁶ Institute of Space Science, Str. Atomistilor, nr. 409 Măgurele, Ilfov, 077125, Romania
- ⁹⁷ Consejo Superior de Investigaciones Científicas, Calle Serrano 117, 28006 Madrid, Spain
- ⁹⁸ Universidad de La Laguna, Departamento de Astrofísica, 38206 La Laguna, Tenerife, Spain
- ⁹⁹ Dipartimento di Fisica e Astronomia "G. Galilei", Università di Padova, Via Marzolo 8, 35131 Padova, Italy
- ¹⁰⁰ Institut für Theoretische Physik, University of Heidelberg, Philosophenweg 16, 69120 Heidelberg, Germany
- ¹⁰¹ Institut de Recherche en Astrophysique et Planétologie (IRAP), Université de Toulouse, CNRS, UPS, CNES, 14 Av. Edouard Belin, 31400 Toulouse, France
- ¹⁰² Université St Joseph; Faculty of Sciences, Beirut, Lebanon
- ¹⁰³ Departamento de Física, FCFM, Universidad de Chile, Blanco Encalada 2008, Santiago, Chile
- ¹⁰⁴ Universität Innsbruck, Institut für Astro- und Teilchenphysik, Technikerstr. 25/8, 6020 Innsbruck, Austria
- ¹⁰⁵ Institut d'Estudis Espacials de Catalunya (IEEC), Edifici RDIT, Campus UPC, 08860 Castelldefels, Barcelona, Spain
- ¹⁰⁶ Satlantis, University Science Park, Sede Bld 48940, Leioa-Bilbao, Spain
- ¹⁰⁷ Institute of Space Sciences (ICE, CSIC), Campus UAB, Carrer de Can Magrans, s/n, 08193 Barcelona, Spain
- ¹⁰⁸ Instituto de Astrofísica e Ciências do Espaço, Faculdade de Ciências, Universidade de Lisboa, Tapada da Ajuda, 1349-018 Lisboa, Portugal
- ¹⁰⁹ Cosmic Dawn Center (DAWN)
- ¹¹⁰ Niels Bohr Institute, University of Copenhagen, Jagtvej 128, 2200 Copenhagen, Denmark
- ¹¹¹ Universidad Politécnica de Cartagena, Departamento de Electrónica y Tecnología de Computadoras, Plaza del Hospital 1, 30202 Cartagena, Spain
- ¹¹² Infrared Processing and Analysis Center, California Institute of Technology, Pasadena, CA 91125, USA
- ¹¹³ Dipartimento di Fisica e Scienze della Terra, Università degli Studi di Ferrara, Via Giuseppe Saragat 1, 44122 Ferrara, Italy
- ¹¹⁴ Istituto Nazionale di Fisica Nucleare, Sezione di Ferrara, Via Giuseppe Saragat 1, 44122 Ferrara, Italy
- ¹¹⁵ INAF, Istituto di Radioastronomia, Via Piero Gobetti 101, 40129 Bologna, Italy
- ¹¹⁶ Astronomical Observatory of the Autonomous Region of the Aosta Valley (OAVdA), Loc. Lignan 39, I-11020, Nus (Aosta Valley), Italy
- ¹¹⁷ Department of Physics, Oxford University, Keble Road, Oxford OX1 3RH, UK
- ¹¹⁸ Instituto de Astrofísica de Canarias (IAC); Departamento de Astrofísica, Universidad de La Laguna (ULL), 38200, La Laguna, Tenerife, Spain
- ¹¹⁹ Université PSL, Observatoire de Paris, Sorbonne Université, CNRS, LERMA, 75014, Paris, France
- ¹²⁰ Université Paris-Cité, 5 Rue Thomas Mann, 75013, Paris, France
- ¹²¹ Department of Mathematics and Physics E. De Giorgi, University of Salento, Via per Arnesano, CP-I93, 73100, Lecce, Italy
- ¹²² INFN, Sezione di Lecce, Via per Arnesano, CP-193, 73100, Lecce, Italy
- ¹²³ INAF-Sezione di Lecce, c/o Dipartimento Matematica e Fisica, Via per Arnesano, 73100, Lecce, Italy
- ¹²⁴ ICL, Junia, Université Catholique de Lille, LITL, 59000 Lille, France
- ¹²⁵ ICSC - Centro Nazionale di Ricerca in High Performance Computing, Big Data e Quantum Computing, Via Magnanelli 2, Bologna, Italy
- ¹²⁶ Instituto de Física Teórica UAM-CSIC, Campus de Cantoblanco, 28049 Madrid, Spain
- ¹²⁷ CERCA/ISO, Department of Physics, Case Western Reserve University, 10900 Euclid Avenue, Cleveland, OH 44106, USA
- ¹²⁸ Technical University of Munich, TUM School of Natural Sciences, Physics Department, James-Franck-Str. 1, 85748 Garching, Germany
- ¹²⁹ Max-Planck-Institut für Astrophysik, Karl-Schwarzschild-Str. 1, 85748 Garching, Germany
- ¹³⁰ Laboratoire Univers et Théorie, Observatoire de Paris, Université PSL, Université Paris Cité, CNRS, 92190 Meudon, France
- ¹³¹ Departamento de Física Fundamental. Universidad de Salamanca. Plaza de la Merced s/n. 37008 Salamanca, Spain
- ¹³² Université de Strasbourg, CNRS, Observatoire astronomique de Strasbourg, UMR 7550, 67000 Strasbourg, France
- ¹³³ Center for Data-Driven Discovery, Kavli IPMU (WPI), UTIAS, The University of Tokyo, Kashiwa, Chiba 277-8583, Japan
- ¹³⁴ Dipartimento di Fisica - Sezione di Astronomia, Università di Trieste, Via Tiepolo 11, 34131 Trieste, Italy
- ¹³⁵ California Institute of Technology, 1200 E California Blvd, Pasadena, CA 91125, USA
- ¹³⁶ Department of Physics & Astronomy, University of California Irvine, Irvine CA 92697, USA
- ¹³⁷ Kapteyn Astronomical Institute, University of Groningen, PO Box 800, 9700 AV Groningen, The Netherlands
- ¹³⁸ Departamento Física Aplicada, Universidad Politécnica de Cartagena, Campus Muralla del Mar, 30202 Cartagena, Murcia, Spain
- ¹³⁹ Instituto de Física de Cantabria, Edificio Juan Jordá, Avenida de los Castros, 39005 Santander, Spain
- ¹⁴⁰ Observatorio Nacional, Rua General Jose Cristino, 77-Bairro Imperial de Sao Cristovao, Rio de Janeiro, 20921-400, Brazil
- ¹⁴¹ Institute of Cosmology and Gravitation, University of Portsmouth, Portsmouth PO1 3FX, UK
- ¹⁴² Department of Computer Science, Aalto University, PO Box 15400, Espoo, FI-00 076, Finland
- ¹⁴³ Instituto de Astrofísica de Canarias, c/ Via Lactea s/n, La Laguna 38200, Spain. Departamento de Astrofísica de la Universidad de La Laguna, Avda. Francisco Sanchez, La Laguna, 38200, Spain
- ¹⁴⁴ Caltech/IPAC, 1200 E. California Blvd., Pasadena, CA 91125, USA
- ¹⁴⁵ Ruhr University Bochum, Faculty of Physics and Astronomy, Astronomical Institute (AIRUB), German Centre for Cosmological Lensing (GCCL), 44780 Bochum, Germany
- ¹⁴⁶ Department of Physics and Astronomy, Vesilinnantie 5, 20014 University of Turku, Finland
- ¹⁴⁷ Serco for European Space Agency (ESA), Camino bajo del Castillo, s/n, Urbanizacion Villafranca del Castillo, Villanueva de la Cañada, 28692 Madrid, Spain
- ¹⁴⁸ ARC Centre of Excellence for Dark Matter Particle Physics, Melbourne, Australia
- ¹⁴⁹ Centre for Astrophysics & Supercomputing, Swinburne University of Technology, Hawthorn, Victoria 3122, Australia
- ¹⁵⁰ Department of Physics and Astronomy, University of the Western Cape, Bellville, Cape Town, 7535, South Africa
- ¹⁵¹ DAMTP, Centre for Mathematical Sciences, Wilberforce Road, Cambridge CB3 0WA, UK
- ¹⁵² Kavli Institute for Cosmology Cambridge, Madingley Road, Cambridge, CB3 0HA, UK
- ¹⁵³ Department of Astrophysics, University of Zurich, Winterthurerstrasse 190, 8057 Zurich, Switzerland
- ¹⁵⁴ Department of Physics, Centre for Extragalactic Astronomy, Durham University, South Road, Durham, DH1 3LE, UK

- ¹⁵⁵ IRFU, CEA, Université Paris-Saclay 91191 Gif-sur-Yvette Cedex, France
- ¹⁵⁶ Oskar Klein Centre for Cosmoparticle Physics, Department of Physics, Stockholm University, Stockholm, SE-106 91, Sweden
- ¹⁵⁷ Astrophysics Group, Blackett Laboratory, Imperial College London, London SW7 2AZ, UK
- ¹⁵⁸ Univ. Grenoble Alpes, CNRS, Grenoble INP, LPSC-IN2P3, 53, Avenue des Martyrs, 38000, Grenoble, France
- ¹⁵⁹ INAF-Osservatorio Astrofisico di Arcetri, Largo E. Fermi 5, 50125, Firenze, Italy
- ¹⁶⁰ Dipartimento di Fisica, Sapienza Università di Roma, Piazzale Aldo Moro 2, 00185 Roma, Italy
- ¹⁶¹ Centro de Astrofísica da Universidade do Porto, Rua das Estrelas, 4150-762 Porto, Portugal
- ¹⁶² HE Space for European Space Agency (ESA), Camino bajo del Castillo, s/n, Urbanizacion Villafranca del Castillo, Villanueva de la Cañada, 28692 Madrid, Spain
- ¹⁶³ Department of Astrophysical Sciences, Peyton Hall, Princeton University, Princeton, NJ 08544, USA
- ¹⁶⁴ INAF-Osservatorio Astronomico di Brera, Via Brera 28, 20122 Milano, Italy, and INFN-Sezione di Genova, Via Dodecaneso 33, 16146, Genova, Italy
- ¹⁶⁵ Theoretical astrophysics, Department of Physics and Astronomy, Uppsala University, Box 515, 751 20 Uppsala, Sweden
- ¹⁶⁶ Mathematical Institute, University of Leiden, Einsteinweg 55, 2333 CA Leiden, The Netherlands
- ¹⁶⁷ Institute of Astronomy, University of Cambridge, Madingley Road, Cambridge CB3 0HA, UK
- ¹⁶⁸ Space physics and astronomy research unit, University of Oulu, Pentti Kaiteran katu 1, FI-90014 Oulu, Finland
- ¹⁶⁹ Department of Physics and Astronomy, Lehman College of the CUNY, Bronx, NY 10468, USA
- ¹⁷⁰ American Museum of Natural History, Department of Astrophysics, New York, NY 10024, USA
- ¹⁷¹ Center for Computational Astrophysics, Flatiron Institute, 162 5th Avenue, 10010, New York, NY, USA

Appendix A: Impact of lack of companions in training set on LEMON performance

To further check how the completeness of the training set influences both the predictions and the uncertainties of LEMON, we also trained the algorithm only on the lenses without companions. We split the lenses into 40 000 lenses for the training set, 5000 lenses for the validation set, and 5000 lenses for the test set. We then trained LEMON with the same procedure as described in Sect. 4.1, and then tested on a companions test set formed by 5000 randomly extracted lenses from the 50 000 lenses with companions.

The recovery from the model trained without companions in the training set of the parameters for the companions test set is shown in Fig. A.1. From the figure, we can see that the Einstein radius is completely unrecovered, with a very strong bias towards higher predicted radii ($\mu \approx 1''$) and a very low value of the coefficient of determination, $R^2 = -14.81$, indicating a poor fit. This suggests that the presence of companions heavily affects the recovery of the Einstein radius, potentially because the contaminants are confused with arc features, or because gravitational effects from the companions alter the lensing characteristics of the images, or both. The axis ratio shows a slightly positive value of R^2 , and a systematic underestimate of the predictions, as seen from the metrics, with $\mu = -0.08$ and $\sigma^- = 0.14$. This indicates that contaminants have a slight effect on the recovery of the lens shape, likely introducing slight distortions of the image that LEMON was not trained to accommodate. The position angle appears to be well recovered, implying that contaminants have practically no effect on the recovery of this parameter. Although the lens effective radius shows a near-zero mean bias, its R^2 of -0.47 and high upper scatter of $\sigma^+ = 0''.21$ highlight that a high scatter induced by the light of the contaminants reduces the model's ability to predict the effective radius, overestimating systematically the size of the galaxy. The lens Sérsic index shows a very large scatter, with $\text{NMAD} = 1.07$, reflecting LEMON's difficulty in recovering the light profile slope, potentially due to additional sources of light in the image that confuse the network. Finally, while the magnitude is the best recovered parameter, with a coefficient of determination $R^2 = 0.77$, it is systematically underestimated ($\mu = -0.29$), indicating that the brightness of contaminants causes LEMON to interpret lenses as brighter than they actually are.

Appendix B: Recovery of Einstein mass

As a side test, we trained LEMON to recover the Einstein mass parameter, defined as the total lens mass enclosed within the largest critical curve. This parameter is the effective total mass responsible for the observed lensing effect.

For any axisymmetric lens model, the Einstein mass is related to the (circularised) Einstein radius via the formula

$$R_{\text{Ein}} = \sqrt{\frac{D_{\text{ds}}}{D_{\text{s}}D_{\text{d}}} \frac{4GM_{\text{Ein}}}{c^2}}, \quad (\text{B.1})$$

where D_{ds} is the source-lens distance, D_{d} is the distance between the observer and the lens and D_{s} is the distance between the observer and the source. Notice that these distances are angular diameter distances, and thus depend on the redshifts of the source and the lens. We thus expect $M_{\text{Ein}} \propto R_{\text{Ein}}^2$.

The recovery of the Einstein mass for the test set lenses is shown in Fig. B.1, with the associated trends for bias and NMAD

shown in the lower two panels. From the figure, we can see that the Einstein mass is well recovered over all the lens mass range. It should be noted that this is not expected: given the implicit dependence of Eq. (B.1) from the redshifts of source and lens, which we did not train the network to recover, the network should have difficulty in recovering the values of Einstein mass through the value of the Einstein radius.

We conjecture that the correct recovery could be due to the fact that the network is learning known or unknown strong correlations between some lensing features and the Einstein mass values, bypassing the need for direct inference of redshift values. Some of these features could be lensing distortion patterns (larger Einstein masses produce more pronounced arcs), size and spread of the lensed images (larger Einstein masses produce wider separations of the lensed images), and brightness of the arcs (larger Einstein masses focus light more intensely, which affects the intensity profiles of the arcs in the image). The network could also be learning implicit correlations between features related to the lens redshift, such as the relative brightness of source and lens, and the redshift of the lens itself. The network could then use these correlations to create a Bayesian mapping that reproduces the relation (B.1), by learning a distribution of possible mappings between Einstein radius and Einstein mass. Thus, when making predictions, the network sees a particular arc size that often correlates with a higher Einstein mass, and gives a value that peaks around the higher value, with smaller or larger uncertainty associated to how often the value of R_{Ein} is associated to a certain value of M_{Ein} in the training phase.

Figure B.2 shows the recovery of the Einstein mass for the SLACS Euclidised lenses sample, which is the only one that has values of Einstein mass reported (Auger et al. 2009, table 4). The recovery of the parameter shows a systematic overestimation, with a mean bias of $\mu = 0.23$. This is similar, but slightly larger, to the bias for the recovery of the Einstein radius for the Euclidised lenses.

To further investigate the origin of this systematic effect, in Fig. B.3 we show the correlation between the Einstein mass and the Einstein radius. For a fixed redshift, we expect ideally a single power-law curve, corresponding to Eq. (B.1) with fixed values of D_{ds} , D_{s} and D_{d} . For different redshifts, in log space we expect a family of curves with fixed slope and varying y -intercept, which is what we see in the figure with the training set region. The figure shows that the region of the training set corresponding to the minimum and maximum redshifts of the SLACS sample aligns with the lower boundary of the training set area, where most of the SLACS sample is concentrated. The ERO lenses from *Euclid*, instead, lie fully within the training-set parameter space, which could explain the better recovery of the Einstein radius for these lenses.

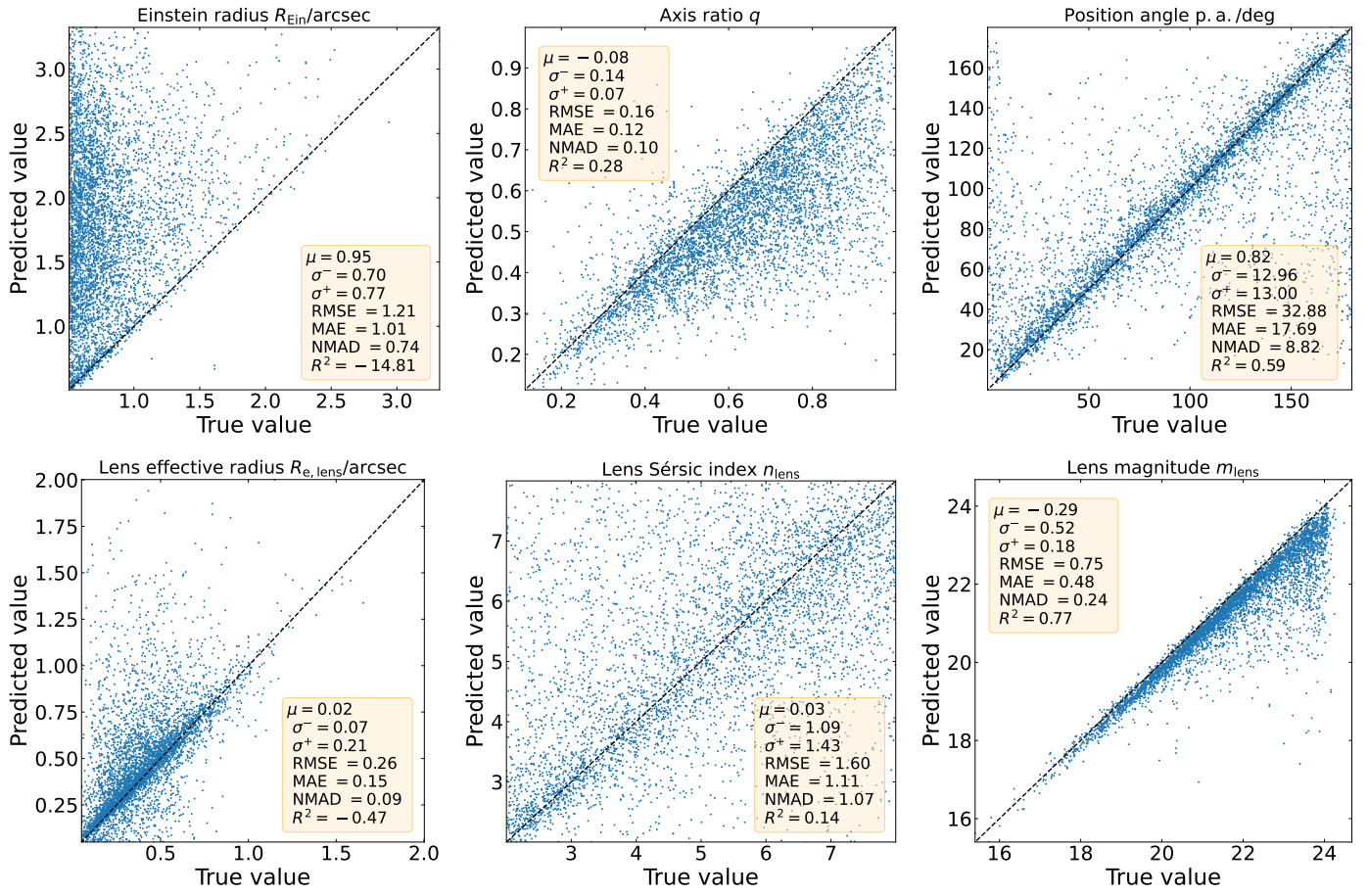


Fig. A.1. Same as Fig. 4, but by using LEMON trained only on non companion lenses and using lenses with companions as the test set.

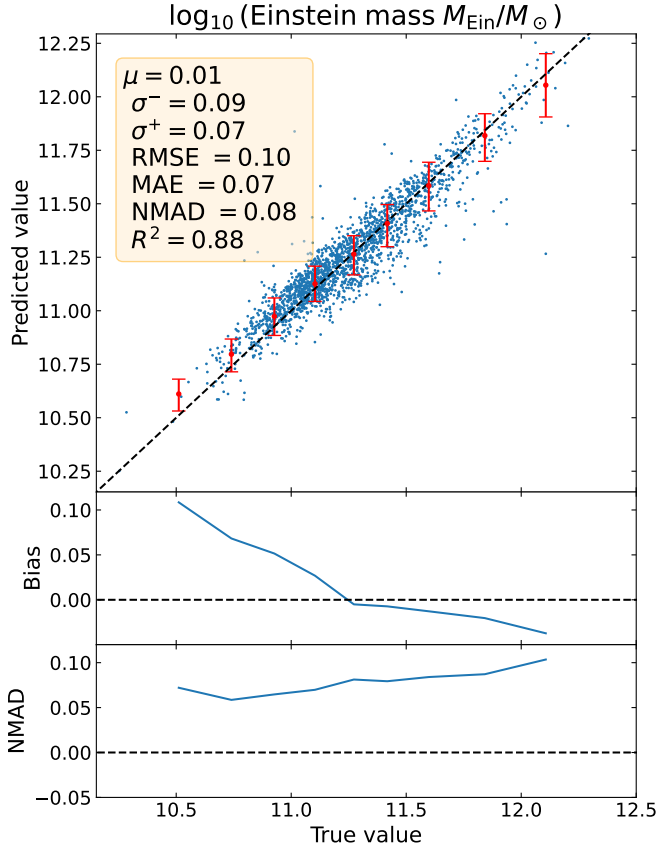


Fig. B.1. Same as Fig. 4, but for the Einstein mass parameter.

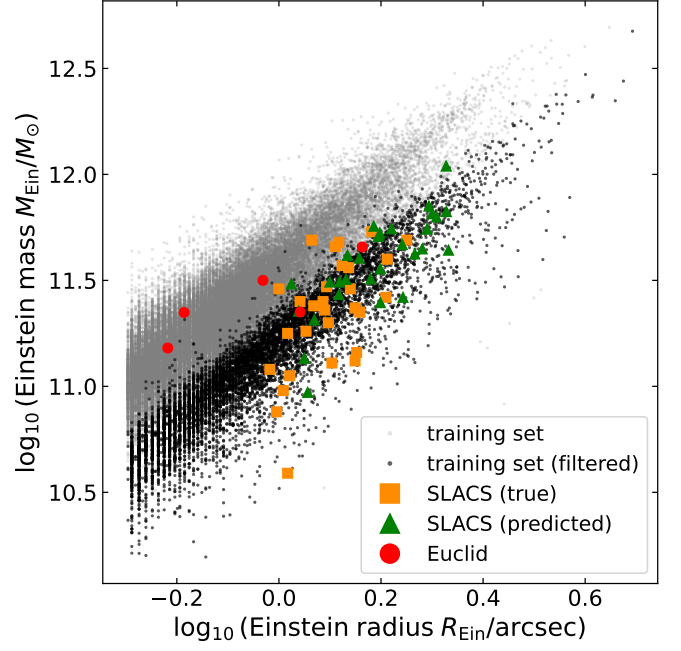


Fig. B.3. Einstein mass as a function of Einstein radius. Grey points are the values for the training set, with black points corresponding to those lenses of the training sample having values of lens redshift within the redshift range of the SLACS sample. Orange squares are the literature parameter values for SLACS lenses, while green triangles are the SLACS predicted values from LEMON. Blue points correspond to the predicted values from LEMON for Euclid ERO lenses considered in Fig. 12.

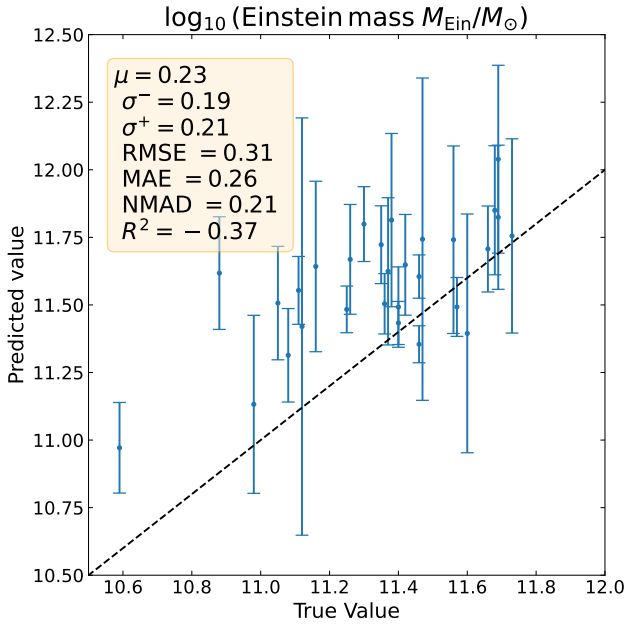


Fig. B.2. Recovery of the Einstein mass parameter for the Euclidised SLACS lenses, showing how well the predicted parameter from LEMON (y coordinate) reproduces the corresponding true value (x coordinate), obtained from Auger et al. (2009).